COMPUTATIONAL ALGORITHMS FOR AUTOMATED EARLY DIAGNOSIS OF ORAL CANCER BASED ON MULTISPECTRAL FLUORESCENCE LIFETIME IMAGING ENDOSCOPY

A Dissertation

by

ELVIS DE JESUS DURAN SIERRA

Submitted to the Office of Graduate and Professional Studies of
Texas A&M University
in partial fulfillment of the requirements for the degree of

DOCTOR OF PHILOSOPHY

Chair of Committee,	Javier Jo
Co-Chair of Committee,	Vladislav Yakovlev
Committee Members,	Kristen Maitland
	Zenon Medina-Cetina
Head of Department,	Mike McShane

May 2020

Major Subject: Biomedical Engineering

ABSTRACT

Oral cancer is one of the most common types of cancer in the US, killing around 8,000 people each year. Patients diagnosed at advanced stages have only a 40% chance of survival and commonly require painful and highly invasive surgery to remove parts of the oral cavity. In contrast, patients diagnosed early usually require minor surgery and have an 84% chance of survival. Therefore, early detection holds great promise for improving both the survival rate and quality of life of these patients. Unfortunately, only three in ten patients are diagnosed at early stages since benign oral lesions are often difficult to distinguish from early stage cancer. Moreover, tissue from a biopsy may register as benign, but the surrounding tissue that was not biopsied can be cancerous and remain undiagnosed, resulting in increased odds of local recurrence and lower survival rates. Hence, there is an urgent need for technologies for accurate, fast, and reliable screening of oral cancer. This dissertation addresses these challenges in the diagnosis of oral cancer and precancer by making use of an optical technology called Fluorescence Lifetime Imaging (FLIM) endoscopy for the non-invasive imaging of clinically suspicious oral lesions in patients. Multispectral autofluorescence lifetime images of benign, precancerous, and cancerous oral lesions from 125 patients were acquired in vivo using a novel multispectral FLIM endoscope. These images were processed to generate widefield maps of biochemical and metabolic autofluorescence biomarkers of oral cancer and precancer. Statistical analyses applied to the quantified multispectral autofluorescence biomarkers indicated their potential to provide contrast between precancerous/cancerous vs. healthy oral tissue and precancerous/cancerous vs. benign oral tissue. Machine learning algorithms based on the most promising autofluorescence biomarkers of oral cancer and precancer were designed to discriminate precancerous/cancerous oral lesions vs. healthy oral tissue, and precancerous/cancerous vs. benign oral lesions. The results of this innovative study demonstrate the potentials of a computer-aided detection system based on endogenous multispectral autofluorescence endoscopy as a novel non-invasive clinical tool for oral cancer and precancer screening.

DEDICATION

To my lovely wife Pilar, my daughters Jimena and Madeleine, and my parents Elvis and Silvia

CONTRIBUTORS AND FUNDING SOURCES

Contributors

This work was supported by a dissertation committee consisting of Professors Javier Jo (chair), Vladislav Yakovlev (co-chair), and Kristen Maitland of the Department of Biomedical Engineering and Professor Zenon Medina of the Department of Civil Engineering.

The data acquired for this project was provided by Dr. Rodrigo Cuenca-Martinez, Dr. Shuna Cheng, and Dr. Bilal Malik . Data analysis and interpretation were conducted by the student and by Dr. Javier Jo.

All other work conducted for the dissertation was completed by the student independently.

Funding Sources

Graduate study was supported by a fellowship from Consejo Nacional de Ciencia y Tecnologia (CONACYT). This project was supported by the National Institutes of Health (grants R01CA138653, 1R01CA218739). This work was also made possible by the grant NPRP8-1606-3-322 from the Qatar National Research Fund (a member of Qatar Foundation).

NOMENCLATURE

FLIM	Fluorescence Lifetime Imaging
MPM-FLIM	Multiphoton Fluorescence Lifetime Imaging
TRFS	Time-Resolved Fluorescence Spectroscopy
AFS	Autofluorescence Spectroscopy
CFM	Confocal Fluorescence Microscopy
SLS	Synchronous Luminescence Spectroscopy
ESS	Elastic Scattering Spectroscopy
OCT	Optical Coherence Tomograhpy
RS	Raman Spectroscopy
HSI	Hyperspectral Imaging
NADH	Nicotinamide Adenine Dinucleotide
FAD	Flavin Adenine Dinucleotide
SCC	Squamous Cell Carcinoma
OSCC	Oral Squamous Cell Carcinoma
HNSCC	Head and Neck Squamous Cell Carcinoma
WDSCC	Well-Differentiated Squamous Cell Carcinoma
MILD-DYS	Mild Dysplasia
MOD-DYS	Moderate Dysplasia
HG-DYS	High-Grade Dysplasia
CIS	Carcinoma In Situ
FOV	Field Of View
FIR	Fluorescence Impulse Response

IRF	Instrument Response Function
MSE	Mean Squared Error
CAD	Computer Aided Detection
LDA	Linear Discriminant Analysis
DLDA	Diagonal Linear Discriminant Analysis
QDA	Quadratic Discriminant Analysis
DQDA	Diagonal Quadratic Discriminant Analysis
SVM	Support Vector Machines
LOGREG	Logistic Regression
ANN	Artificial Neural Network
CNN	Convolutional Neural Network
LOOCV	Leave One Out Cross Validation
ROC	Receiver Operating Characteristic
AUC	Area Under Curve
PPV	Positive Predictive Value
NPV	Negative Predictive Value

TABLE OF CONTENTS

Page

LIST OF FIGURES

LIST OF TABLES

1. INTRODUCTION

This dissertation addresses two big challenges in the clinical diagnosis of oral cancer: Incomplete tumor resection (Sections 2 and 3) and early detection of oral cancer (Sections 4 and 5).

In Section 2, we report the first demonstration of biochemical and metabolic clinical imaging of precancerous and cancerous oral lesions using widefield multispectral fluorescence lifetime imaging (FLIM) endoscopy. In vivo FLIM images of precancerous and cancerous oral lesions from patients were acquired. Maps of biochemical and metabolic autofluorescence biomarkers of oral cancer and precancer were generated. Statistical analyses applied to them demonstrated their potential to discriminate precancerous/cancerous lesions from healthy oral epithelial tissue.

Section 3 investigates a computational framework for a computer aided detection (CAD) system designed for the classification of precancerous/cancerous lesions vs. healthy oral tissue. Multispectral autofluorescence feature maps of precancerous, cancerous, and healthy oral tissues were computed and used within machine learning algorithms. The proposed CAD system successfully differentiated precancerous and cancerous oral lesions from healthy oral tissue with competent levels of sensitivity and specificity.

In Section 4, we report a subsequent analysis derived from Section 2 in benign, precancerous, and cancerous oral lesions. As in Section 2, multiparametric FLIM feature maps were generated for each of the imaged benign, precancerous and cancerous oral lesions from patients. Statistical analyses performed on the computed FLIM feature maps demonstrated their potential to discriminate precancerous/cancerous from benign oral lesions.

Finally, Section 5 reports a computational framework for a CAD system designed for the classification of precancerous/cancerous vs. benign oral lesions. Multispectral autofluorescence feature maps of precancerous, cancerous, and benign oral lesions were generated and used within machine learning algorithms. The proposed CAD system successfully distinguished precancerous/cancerous from benign oral lesions with decent levels of sensitivity and specificity.

2. CLINICAL LABEL-FREE BIOCHEMICAL AND METABOLIC FLUORESCENCE LIFETIME ENDOSCOPIC IMAGING OF PRECANCEROUS AND CANCEROUS ORAL LESIONS *

2.1 Introduction

About 53,260 new cases of cancer of the oral cavity and pharynx will be diagnosed in the US in 2020, and an estimate of 10,750 people will die of these cancers during the same year [1]. Current standard treatments for oral cancer are surgical resection with or without radiation or chemotherapy [1, 2]. During tumor surgical resection, however, surgeons typically rely on visual inspection and palpation to demarcate the subtle interface at the margin between malignant and normal oral tissue [3]. As a result, incomplete tumor resections occur in up to 85% of cases [4, 5], leading to increased odds of local recurrences and regional neck metastases, as well as lower survival rates [6]. The standard technique to overcome this limitation is intraoperative histopathological evaluation of frozen sections from random tissue biopsies, which is not only labor-intensive and time-consuming, but also prone to sampling error and has limited specificity [7, 8].

The human oral mucosa consists of two major layers: Stratified squamous epithelium and lamina propria or connective tissue. The development of squamous cell carcinoma (SCC) causes morphological, functional, and biochemical alterations within these tissue layers, which can modulate the autofluorescence properties of the oral epithelial tissue. Specifically, the levels of two metabolic cofactors and endogenous fluorophores, the reduced-form nicotinamide adenine dinucleotide (NADH) and flavin adenine dinucleotide (FAD), can change as oral cancer develops [9, 10, 11]. The optical redox ratio, typically defined as the ratio of fluorescence intensity of NADH to FAD, is sensitive to changes in the cellular metabolic rate [12, 13, 14, 15]. Increased cellular metabolic activity, a hallmark of neoplastic cell transformation, is usually attributed to a decrease in the optical redox ratio [16]. In addition, the fluorescence lifetime of these metabolic

*Reprinted with permission from "Clinical label-free biochemical and metabolic fluorescence lifetime endoscopic imaging of precancerous and cancerous oral lesions" by Elvis Duran-Sierra, et al. 2020. *Oral Oncology*, Volume 105, 104635, Copyright [2020] by Elsevier Ltd.

cofactors are sensitive to protein binding, thus to cellular metabolic pathways involving NADH and FAD [17]. As a result, the carcinogenesis process causes changes in both NADH and FAD fluorescence lifetimes [18]. Finally, oral cancer development also leads to extracellular matrix remodeling occurring within the lamina propria, which together with concurring epithelium thickening, result in a decrease in connective tissue autofluorescence that can be measured [19]. Therefore, interrogation of NADH, FAD and collagen autofluorescence could provide optical biomarkers of oral epithelial cancer.

Several studies have explored the use of autofluorescence spectroscopy and imaging to identify biomarkers of oral SCC. Gillenwater et al. observed increased epithelial autofluorescence and decreased connective tissue autofluorescence in dysplastic vs. normal oral tissue upon ultraviolet excitation [20]. Rosin et al. used fluorescence visualization (FV) in an in vivo study in 20 patients with oral SCC and carcinoma in situ (CIS) to collect the autofluorescence at an >475 nm emission spectral band, and found that all SCC and CIS tumors showed FV loss relative to normal tissue; moreover, in 19 cases the loss in autofluorescence signal extended 4-25 mm in at least one direction beyond the clinically visible tumor [21]. In an in vivo study, Huang et al., using a two-channel autofluorescence device targeting NADH and FAD autofluorescence, reported discrimination of precancerous and cancerous lesions vs. healthy oral mucosa with levels of sensitivity and specificity of $\sim$92% and $\sim$75%, respectively [22].

Time-resolved fluorescence spectroscopy (TRFS) and fluorescence lifetime imaging microscopy (FLIM), which allows measuring the fluorescence lifetime of samples, can provide additional sample characterization. Singaravelu et al. performed an ex vivo TRFS study in 15 premalignant and 15 normal oral tissue samples from patients, and reported a significantly shorter lifetime associated to free NADH in premalignant vs. normal oral tissue [23]. In an ex vivo multiphoton FLIM study using human oral tissue samples, Skala et al. reported shorter NADH and FAD average fluorescence lifetimes, and a lower redox ratio in SCC relative to normal oral tissue [24]. Farwell et al. performed an in vivo TRFS study in nine patients with suspected HNSCC and found lower fluorescence intensity across all wavelengths between 360 nm and 610 nm and a shorter lifetime at the

440-470 nm band in head and neck squamous cell carcinoma (HNSCC) vs. normal [25]. In an in vivo FLIM study performed in 10 patients with HNSCC, Marcu et al. reported lower fluorescence intensity and shorter average lifetime associated to NADH in HNSCC compared to healthy oral tissue [2].

Encouraged by these pioneering studies and taking advantage of novel multispectral FLIM endoscopy systems recently developed for imaging the oral mucosa [26], we demonstrate in this in vivo human study the capabilities of endogenous wide-field multispectral FLIM endoscopy in differentiating oral SCC/epithelial dysplasia from normal oral tissue; and provide the basis for using autofluorescence biomarkers in the future for rapid and accurate determination of margin involvement in the operation room.

2.2 Methods

A schematic summarizing the methodology used in this study is presented in Figure 2.1 and described in the following sections.

2.2.1 Clinical Endoscopic Multispectral FLIM Imaging of Oral Lesions

In vivo clinical endogenous multispectral FLIM images of dysplastic and cancerous oral lesions were acquired following an imaging protocol approved by the Institutional Review Board at Texas A&M University. For this study, 39 patients, scheduled for tissue biopsy examination of suspicious oral epithelial precancerous or cancerous lesions, were recruited. Following clinical examination of the patient's oral cavity by an experienced oral pathologist (Y.S. Lisa Cheng and John Wright, Texas A&M College of Dentistry, Dallas, TX, USA), endogenous FLIM images were acquired from the suspicious oral lesion and a clinically normal-appearing area in the corresponding contralateral anatomical side, using a FLIM endoscope prototype previously reported [26]. With this multispectral FLIM endoscope prototype, tissue autofluorescence induced with a pulsed laser (355 nm, 1 ns pulse width, $\sim 1 \mu$J/pulse at the tissue) was imaged at the emission spectral bands of 390 $\pm$ 20 nm, 452 $\pm$ 22.5 nm, and > 500 nm, which were selected to preferentially measure collagen, NADH, and FAD autofluorescence, respectively [26]. In order to perform in vivo imag-

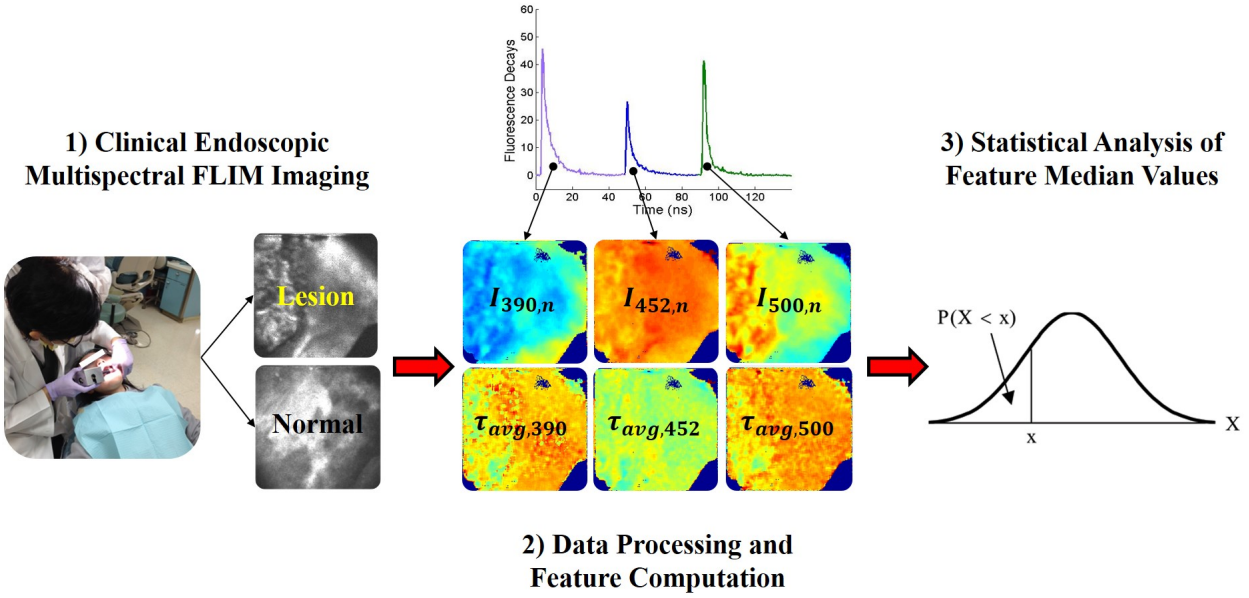

Figure 2.1: Schematic depicting the methodology of this study. First, multispectral FLIM endoscopic imaging of oral lesions is performed in a clinical setting. Second, the data is processed yielding multi-parametric FLIM feature images. Finally, statistical analysis is performed on the feature image median value to assess difference in their distributions between precancerous/cancerous and normal groups.

ing in a safe manner, the total energy deposited into the patient's oral mucosa was set to at least an order of magnitude lower than the maximum permissible exposure provided by the American National Standards Institute (ANSI) [27]. The time-resolved autofluorescence signal at each pixel of the FLIM images were acquired with a temporal resolution of 160 ps (sampling rate of 6.25 GS/s). Endoscopic multispectral FLIM images were acquired with a circular field-of-view (FOV) of 10 mm in diameter, lateral resolution of $\sim$100μm, and acquisition time of <3 s (total acquisition time for the three emission spectral bands). After acquiring all the multispectral FLIM images from the patient's oral cavity, the tissue biopsy examination procedure was performed following standard clinical protocols and blinded to the FLIM imaging. Each imaged lesion was annotated based on its tissue biopsy histopathological diagnosis. In one case, two images were acquired from a patient who presented two cancerous lesions that were biopsied, resulting in a total of 40 imaged oral lesions. Unfortunately, since the FLIM endoscope system was handled by different users in

Lesion Location	Histopathology Diagnosis			Total Number
	MOD-DYS	HG-DYS	SCC	
Buccal Mucosa	2	1	11	**14**
Tongue	1	0	12	**13**
Gingiva	0	1	7	**8**
Lip	0	0	2	**2**
Mandible	0	0	1	**1**
Maxilla	0	0	1	**1**
Floor of Mouth	0	0	1	**1**
Total Number	**3**	**2**	**35**	**40**

Table 2.1: Distribution of the 40 imaged oral lesions based in both anatomical location and histopathological diagnosis (MOD-DYS: Moderate Dysplasia; HG-DYS: High-Grade Dysplasia; SCC: Squamous Cell Carcinoma)

the clinic, the photodetector gain, which allows to compare the multispectral absolute fluorescence intensity values, was only recorded in 32/40 cases.

The distribution of the 40 imaged oral lesions, based in both anatomical location and histopathological diagnosis, is provided in Table 2.1.

2.2.2 Data Processing and Feature Computation

The multispectral FLIM data is composed of fluorescence intensity temporal decay signals, $y_\lambda(x, y, t)$, measured at each emission spectral band (λ) and each spatial location or image pixel (x, y). Multispectral absolute and normalized fluorescence intensity values were first computed for each pixel as follows. The multispectral absolute fluorescence intensity $I_\lambda(x, y)$ was computed by numerically integrating the fluorescence intensity temporal decay signal:

$$I_\lambda(x, y) = \int y_\lambda(x, y, t)dt \tag{2.1}$$

The multispectral normalized fluorescence intensity $I_{\lambda,n}(x, y)$ was computed from the multispectral absolute fluorescence intensities $I_\lambda(x, y)$ as follows:

$$I_{\lambda,n}(x, y) = \frac{I_\lambda(x, y)}{\sum_\lambda I_\lambda(x, y)} \tag{2.2}$$

In addition, the multispectral fluorescence intensity values enable estimating a parameter related to the tissue metabolic redox-ratio similar to the one originally proposed by Chance [15]:

$$RedoxRatio(x,y) = \frac{I-NADH}{I-FAD} = \frac{I_{452}(x,y)}{I_{500}(x,y)} \tag{2.3}$$

In the context of time-domain FLIM data analysis, the fluorescence decay $y_\lambda(x,y,t)$ measured at each spatial location (x,y) can be modeled as the convolution of the fluorescence impulse response (FIR) $h_\lambda(x,y,t)$ of the sample and the measured instrument response function (IRF) $u_\lambda(t)$:

$$y_\lambda(x,y,t) = u_\lambda(t) * h_\lambda(x,y,t) \tag{2.4}$$

Therefore, to estimate the sample FIR $h_\lambda(x,y,t)$, the measured IRF $u_\lambda(t)$ needs to be temporally deconvolved from the measured fluorescence decay $y_\lambda(x,y,t)$. In this work, temporal deconvolution was performed using a nonlinear least squares iterative reconvolution algorithm [28], in which the FIR was modeled as a bi-exponential function:

$$h_\lambda(x,y,t) = \alpha_{fast,\lambda}(x,y)e^{-t/\tau_{fast,\lambda}(x,y)} + \alpha_{slow,\lambda}(x,y)e^{-t/\tau_{slow,\lambda}(x,y)} \tag{2.5}$$

Here, $\tau_{fast,\lambda}(x,y)$ and $\tau_{slow,\lambda}(x,y)$ represent the time-constant (lifetime) of the fast and slow decay components, respectively. $\alpha_{fast,\lambda}(x,y)$ and $\alpha_{slow,\lambda}(x,y)$ represent the relative contribution of the fast and slow decay components, respectively. The model order (number of exponential components) was determined based on the model-fitting mean squares error (MSE); since the addition of a third component did not reduce the MSE, a model order of two was selected. Finally, the average fluorescence lifetime ($\tau_{avg,\lambda}(x,y)$) for each pixel and emission spectral band were estimated from the FIR $h_\lambda(x,y,t)$ as follows [28]:

$$\tau_{avg,\lambda}(x,y) = \frac{\int t h_\lambda(x,y,t)dt}{\int h_\lambda(x,y,t)dt} \tag{2.6}$$

390 ± 20 nm	**452 ± 22.5 nm**	**>500 nm**
$I_{390,n}(x,y)$	$I_{452,n}(x,y)$	$I_{500,n}(x,y)$
$\tau_{avg,390}(x,y)$	$\tau_{avg,452}(x,y)$	$\tau_{avg,500}(x,y)$
$\tau_{fast,390}(x,y)$	$\tau_{fast,452}(x,y)$	$\tau_{fast,500}(x,y)$
$\tau_{slow,390}(x,y)$	$\tau_{slow,452}(x,y)$	$\tau_{slow,500}(x,y)$
$\alpha_{fast,390}(x,y)$	$\alpha_{fast,452}(x,y)$	$\alpha_{fast,500}(x,y)$
Redox-Ratio (x,y)**:** $I_{452}(x,y)/I_{500}(x,y)$		

Table 2.2: Summary of FLIM-derived features computed per pixel for each spectral channel.

In summary, a total of 16 FLIM-derived features were computed per pixel as summarized in Table 2.2, thus enabling the generation of multi-parametric FLIM feature maps.

2.2.3 Statistical Analysis

As summarized in Table 2.1, the 40 imaged oral lesions corresponded to 5 precancerous (3 MOD-DYS, 2 HG-DYS) and 35 cancerous (SCC) lesions, and each imaged oral lesion region was paired with a corresponding clinically healthy or normal oral tissue region. In order to identify statistical differences in the distribution of image median values of each of the 16 FLIM features from normal (healthy) vs. precancerous or cancerous oral tissue, the following statistical analysis was performed. For each imaged oral tissue region, multi-parametric FLIM maps were generated, in which the 16 FLIM features were computed at each image pixel (as in Figure 2.4). Then, for each FLIM feature map, the median feature value from all pixels was computed; thus, each imaged oral tissue region was represented by a single feature vector composed of the median values of each of the 16 FLIM feature maps. Finally, a two-tailed Wilcoxon signed-rank test was applied to the paired precancerous/cancerous vs. normal median values of each of the 16 FLIM features, with a type-1 error probability of $p<0.05$ for all tests.

2.3 Results

The statistical analysis comparing the feature image median values in MOD-DYS/HG-DYS/SCC vs. the corresponding contralateral normal tissue indicated that 13 FLIM-derived features showed statistically different distributions between the precancerous/cancerous vs. normal oral tissue

groups ($P < 0.05$). Box plots of the feature image median value distributions for each oral tissue group are shown in Figure 2.2.

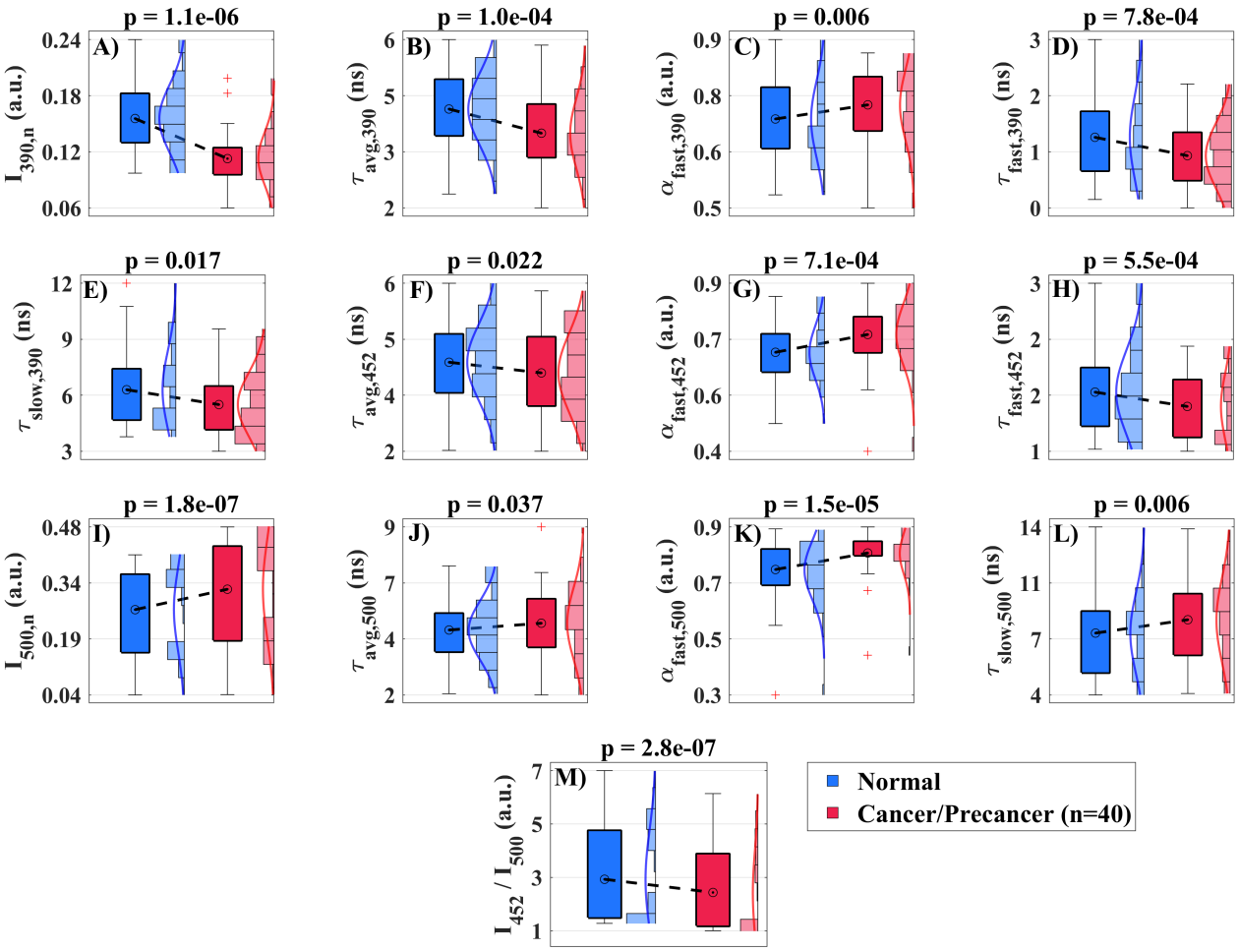

Figure 2.2: Box plots of multispectral FLIM feature image median values of moderate dysplastic (MOD-DYS), high grade dysplastic (HG-DYS), and squamous cell carcinoma (SCC) oral lesions (n=40; red boxes) and their paired contralateral normal tissue (blue boxes). Feature distributions for each population are also shown. P-values resulting from Wilcoxon signed-rank tests are shown on top of each plot.

For a subset of oral lesion samples (n = 32) for which the gain of the photodetector was known, statistical analysis was also performed on the absolute intensity values for each of the three spectral channels comparing MOD-DYS/HG-DYS/SCC vs. normal. Results from these analyses are shown

in Figure 2.3.

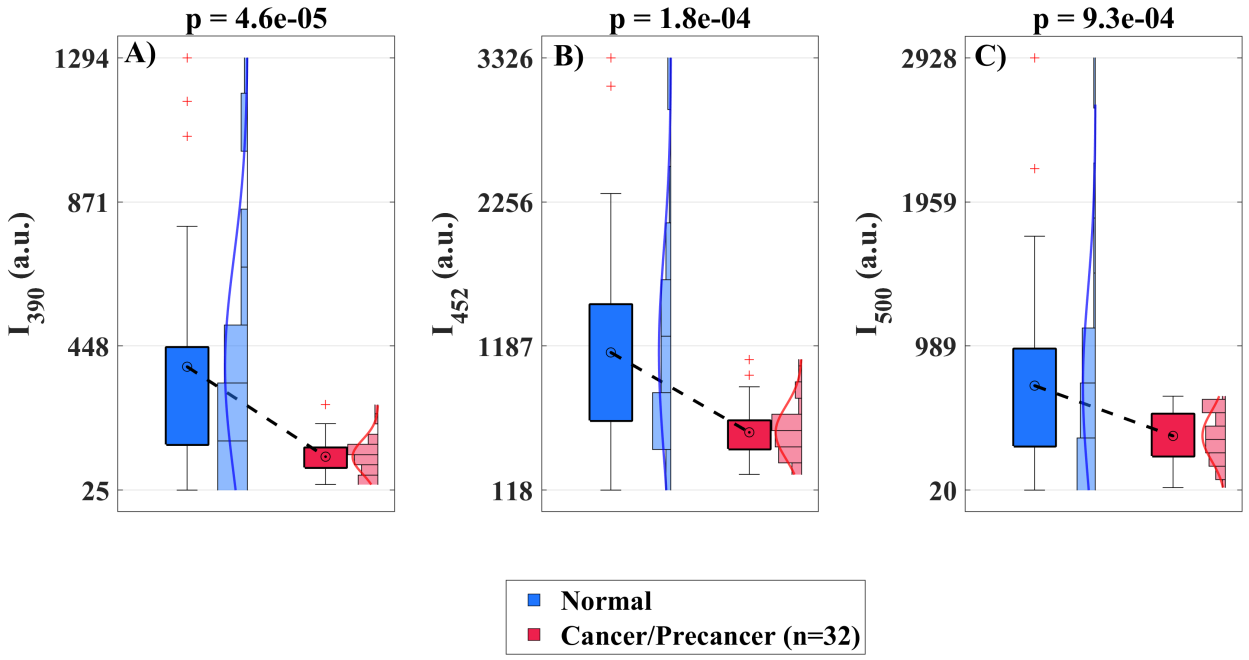

Figure 2.3: Box plots of image median value distributions of absolute fluorescence intensity values for each emission spectral band comparing moderate dysplastic (MOD-DYS), high grade dysplastic (HG-DYS), and squamous cell carcinoma (SCC) oral lesions (n=32; red boxes) to their paired normal references (blue boxes). A statistically significant loss in autofluorescence was observed in precancerous/cancerous oral lesions relative to normal in all spectral channels. P-values resulting from Wilcoxon signed-rank tests are shown on top of each plot.

Multispectral FLIM feature images from a representative lesion corresponding to a SCC of the tongue and its corresponding contralateral normal looking area from the same patient are presented in Figure 2.4. The pixel distributions of each paired FLIM feature map reflected the statistical differences in the image median distribution of each FLIM feature from precancerous/cancerous vs. normal oral tissue.

2.4 Discussion

Using a novel multispectral FLIM endoscope [26], it was possible to image the oral cavity of 39 patients presenting precancerous or cancerous oral lesions. The relatively large field-of-view (∼80

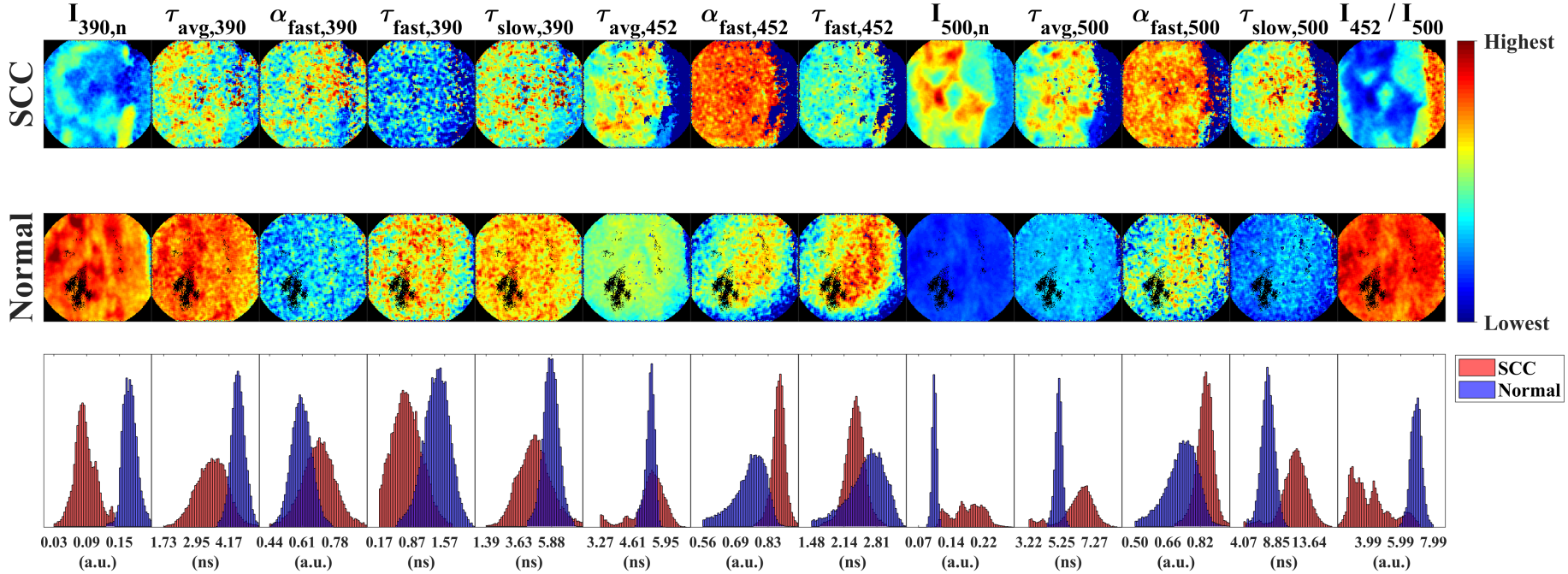

Figure 2.4: Multispectral FLIM feature maps of SCC (top panels) and normal (middle panels) tongue tissue from the same patient. Pixel distributions of normal and SCC maps for each feature are also compared (bottom panels). The trends observed in this representative case are consistent with the statistical findings on the feature image median value distributions from precancerous/cancerous vs. normal oral tissue.

mm^2) and short acquisition time (<3 s per multispectral image) offered by our multispectral FLIM endoscopy system enabled quick and easy in-vivo imaging of oral lesions at the dental clinic. The multispectral FLIM endoscopic images were processed to generate widefield maps of biochemical and metabolic autofluorescence biomarkers of oral precancer and cancer. To the best of our knowledge, this study represents the first demonstration of label-free biochemical and metabolic clinical imaging of precancerous and cancerous oral lesions through widefield multispectral autofluorescence lifetime endoscopy.

Processing of the multispectral FLIM images acquired with our endoscope resulted in widefield maps of different autofluorescence spectral and lifetime features. The statistical analysis applied to each of these autofluorescence features identified several ones (Figure 2.2 and Figure 2.3) that displayed statistically significant differences between precancerous/cancerous vs. healthy oral tissue. In Table 2.3, the statistical trends of the autofluorescence spectral and lifetime features observed in this study are summarized and compared with previously reported observations.

The autofluorescence in oral mucosa induced by an excitation wavelength of 355 nm and measured at the emission spectral band of 390 $\pm$ 20 nm is expected to be predominantly originated from collagen in the lamina propria. Our findings indicated a significant decrease in the normalized autofluorescence intensity at this spectral band in cancerous and precancerous oral lesions relative to healthy oral tissue ($I_{390,n}$, Figure 2.2A), which can be attributed to the breakdown of collagen crosslinks in the connective tissue [19, 29] and the increase in both epithelial thickness and tissue optical scattering accompanying dysplastic or cancerous change [30] and is very much in agreement with previous observations from animal and human studies [20, 25, 31, 32, 33].

Moreover, our findings indicated significantly shorter average ($\tau_{avg,390}$, Figure 2.2B), fast-component ($\tau_{fast,390}$, Figure 2.2D), and slow-component ($\tau_{slow,390}$, Figure 2.2E) lifetimes at the 390 $\pm$ 20 nm emission spectral band in cancerous and precancerous oral lesions compared to healthy oral tissue. To the best of our knowledge, this is the first observation of a faster autofluorescence temporal response at the collagen emission spectral peak in cancerous and precancerous oral lesions. This observation is likely due to the overlap in the emission spectra of collagen and NADH

Emission Channel	Associated Fluorophore	FLIM-Derived Autofluorescence Features	Moderate and High-Grade Dysplasia / SCC vs. Normal	
			Observed Trend	Previous Studies [Ref.]
390 ± 20 nm	**Collagen**	I_{390} $I_{390,n}$	↓ ↓	↓ In Vivo AFS: Hamsters [33] ↓ Ex Vivo CFM: Patients [20] ↓ Ex Vivo SLS: Patients [31] ↓ In Vivo FLIM: Hamsters [32] ↓ In Vivo TRFS: Patients [25]
		$\tau_{avg,390}$	↓	Not Reported
		$\alpha_{fast,390}$	↑	Not Reported
		$\tau_{fast,390}$	↓	Not Reported
		$\tau_{slow,390}$	↓	Not Reported
452 ± 22.5 nm	**NADH**	I_{452} $I_{452,n}$	↓ No Change	↓ In Vivo FLIM: Patients [2] ↓ In Vivo AFS: Hamsters [33] ↓ Ex Vivo SLS: Patients [31] ↓ In Vivo TRFS: Patients [25]
		$\tau_{avg,452}$	↓	↓ In Vivo FLIM: Patients [2] ↓ In Vivo FLIM: Hamsters [32] ↓ Ex Vivo FLIM: Patients [24] ↓ In Vivo TRFS: Patients [25]
		$\alpha_{fast,452}$	↑	Not Reported
		$\tau_{fast,452}$	↓	↓ In Vivo MPM-FLIM: Hamsters [18] ↓ Ex Vivo TRFS: Patients [23]
		$\tau_{slow,452}$	No Change	↓ In Vivo MPM-FLIM: Hamsters [18]
>500 nm	**FAD**	I_{500} $I_{500,n}$	↓ ↑	↑ In Vivo AFS: Hamsters [33] ↑ Ex Vivo CFM: Patients [20] ↑ Ex Vivo SLS: Patients [31] ↑ In Vivo TRFS: Patients [25]
		$\tau_{avg,500}$	↑	↓ Ex Vivo FLIM: Patients [24]
		$\alpha_{fast,500}$	↑	↓ In Vivo MPM-FLIM: Hamsters [18]
		$\tau_{fast,500}$	No Change	↑ In Vivo MPM-FLIM: Hamsters [18]
		$\tau_{slow,500}$	↑	Not Reported
452 / 500 nm	**Redox-Ratio = NADH / FAD**	I_{452}/I_{500}	↓	↓ In Vivo AFS: Hamsters [33] ↓ Ex Vivo FLIM: Patients [24]

Table 2.3: Summary of statistical trends of FLIM-derived features in Moderate and High-Grade Dysplasia/SCC vs. Normal. TRFS: Time-Resolved Fluorescence Spectroscopy; FLIM: Fluorescence Lifetime Imaging; MPM-FLIM: Multiphoton FLIM; AFS: Autofluorescence Spectroscopy; CFM: Confocal Fluorescence Microscopy; SLS: Synchronous Luminescence Spectroscopy

at this band, as a decrease in the slower-decaying collagen signal in precancerous and cancerous epithelial tissue would result in overall faster tissue autofluorescence temporal response mainly modulated by NADH; however, further studies are needed to understand these observations. The observed significantly larger relative contribution of the fast-component ($\alpha_{fast,390}$, Figure 2.2C) is likely due to increased contribution of NADH fluorescence to the acquired signal at this spectral band.

The oral epithelial tissue autofluorescence induced with an excitation wavelength of 355 nm and measured at the emission spectral band of 452 $\pm$ 22.5 nm is expected to be predominantly originated from NADH within oral epithelial cells. Our results indicated significantly shorter average lifetime at the 452 $\pm$ 22.5 nm emission spectral band in cancerous and precancerous oral lesions compared to healthy oral tissue ($\tau_{avg,452}$, Figure 2.2F), consistent with previous observations [2, 24, 25, 32]. Because of the overlap in the emission spectra of collagen and NADH at this spectral band, a decrease in the slower-decaying collagen signal in precancerous and cancerous epithelial tissue would result in overall faster tissue autofluorescence temporal response associated to NADH signal.

Previous studies on animal models of oral cancer using multiphoton FLIM microscopy at $\sim$800 nm two-photon excitation have linked the fast and slow component lifetimes of the epithelial tissue autofluorescence at $\sim$450 nm to intracellular free and bound NADH, respectively [18]. Fast ($\tau_{fast,452}$) and slow ($\tau_{slow,452}$) component lifetimes of the tissue autofluorescence at $\sim$450 nm were also quantified from our widefield FLIM endoscopy images; however, due to the lack of axial resolution of the FLIM endoscope, it is more likely that they reflect epithelial NADH ($\tau_{fast,452}$) and connective tissue collagen ($\tau_{slow,452}$) instead of free/bound NADH. The observed significantly shorter lifetime ($\tau_{fast,452}$, Figure 2.2H) in cancerous and precancerous oral lesions compared to healthy oral tissue might be explained by the increased use of glycolysis in addition to oxidative phosphorylation as complementary metabolic pathways in neoplastic cells [34], as glycolysis requires the reduction of NAD+ into NADH, resulting in increased NADH/NAD+ ratio and quenched NADH fluorescence [35]. The observed significantly larger relative contribution of the

fast-component ($\alpha_{fast,452}$, Figure 2.2G) is likely caused by the decrease in collagen fluorescence associated to the slow component ($\tau_{slow,452}$).

The oral epithelial tissue autofluorescence induced with an excitation wavelength of 355 nm and measured at the emission spectral band > 500 nm is expected to be predominantly originated from FAD within oral epithelial cells. Our findings indicated a significant increase in the normalized autofluorescence intensity at this spectral band ($I_{500,n}$, Figure 2.2I) in cancerous and precancerous oral lesions relative to healthy oral tissue, consistent with previous observations [20, 25, 31, 33]. Oxidative phosphorylation, the most efficient cellular metabolic pathway, requires the oxidation of $FADH_2$ into FAD; thus, the higher metabolic rate of malignant cells would result in higher concentration of mitochondrial FAD, which might explain this observation [35].

Previous studies using multiphoton FLIM microscopy at ~900 nm two-photon excitation have linked the average lifetime of oral tissue autofluorescence imaged at ~500-600 nm to the lifetime of oral epithelial FAD autofluorescence [24], and the fast and slow component lifetimes of oral tissue autofluorescence imaged at a similar emission band to the lifetimes of oral intracellular bound and free FAD autofluorescence, respectively [18]. Average ($\tau_{avg,500}$), fast-component ($\tau_{fast,500}$) and slow-component ($\tau_{slow,500}$) lifetimes of oral tissue autofluorescence at > 500 nm were also quantified from our widefield FLIM endoscopy images. Due to the single-photon 355 nm excitation and broad emission spectral band used in the FLIM endoscope, it is quite possible that the tissue autofluorescence imaged at the > 500 nm spectral band could come not only from FAD but also from NADH and/or porphyrin; thus, it is unlikely that $\tau_{avg,500}$, $\tau_{fast,500}$ and $\tau_{slow,500}$ would only reflect total or free/bound FAD. Nevertheless, although further studies are needed to understand the observed longer $\tau_{avg,500}$ (Figure 2.2J), larger $\alpha_{fast,500}$ (Figure 2.2K) and slower $\tau_{slow,500}$(Figure 2.2L) in cancerous and precancerous oral lesions relative to healthy oral tissue, these results suggest that these endoscopic FLIM features could potentially represent novel autofluorescence biomarkers of oral epithelial dysplasia and cancer.

Since the oral epithelial tissue autofluorescence induced with 355 nm excitation and measured at the emission spectral bands of 452 $\pm$ 22.5 nm and > 500 nm are expected to be predomi-

nantly originated from epithelial NADH and FAD, respectively, the autofluorescence intensity ratio I_{452}/I_{500} can be associated to the optical redox-ratio [15]. Our findings indicated a significant decrease in I_{452}/I_{500} in cancerous and precancerous oral lesions relative to healthy oral tissue (Figure 2.2M), consistent with previous observations [24, 33]. Oxidative phosphorylation requires the oxidation of both NADH and $FADH_2$ molecules, resulting in decreased NADH/FAD redox-ratio [35]. Thus, the observed decreased I_{452}/I_{500} in cancerous and precancerous oral lesions could reflect increased cellular metabolic activity, a hallmark of epithelial cell malignant transformation [16]. Finally, our findings also indicated significantly reduced absolute autofluorescence intensities at all three spectral bands in cancerous and precancerous oral lesions relative to healthy oral tissue (I_{390},I_{452},I_{500}, Figure 2.3), also consistent with previous observations [2, 20, 25, 32, 33].

Three out of 16 FLIM-derived features were not statistically different in precancerous/cancerous lesions vs. normal oral tissue as indicated in Table 2.3. The normalized autofluorescence intensity in channel 452 $\pm$ 22.5 nm ($I_{452,n}$) was not significantly different between premalignant/malignant oral lesions and healthy tissue. As $I_{390,n}$ decreased and $I_{500,n}$ increased in cancerous and precancerous oral lesions, and the three normalized intensities have to add to one, little change in $I_{452,n}$ is expected. The slow component lifetime imaged at this spectral channel ($\tau_{slow,452}$) was not significantly different between premalignant/malignant oral lesions and healthy tissue. The much stronger contribution of NADH in this emission channel might explain the limited effect of the slow-decaying collagen fluorescence associated with $\tau_{slow,452}$. Finally, the fast component lifetime in channel > 500 nm ($\tau_{fast,500}$) was not significantly different in precancerous/cancerous lesions. The much stronger contribution of FAD in this emission channel might explain the limited effect of the fast-decaying NADH fluorescence associated with $\tau_{fast,500}$.

2.4.1 Study Limitations

Although this study demonstrates the capabilities of endogenous multispectral FLIM endoscopy to enable label-free biochemical and metabolic clinical imaging of precancerous and cancerous oral lesions, some important limitations of the study warrant discussion.The multispectral FLIM endoscope used in this study was designed to preferentially interrogate the contributions of collagen,

NADH and FAD in the oral tissue autofluorescence by selecting three spectral channels targeting the emission peak of each of these fluorophores. However, due to 1) the overlap of the emission spectra of these fluorophores, 2) the use of relatively broad spectral emission bands to warranty adequate image quality, 3) the use of a single excitation wavelength, and 4) the lack of axial resolution of the FLIM endoscope, which prevents cellular resolution imaging of the oral epithelial layer independently from the submucosa, specific interrogation of collagen, NADH and FAD was not possible, and it is expected that the fluorescence emission measured at any of the selected emission bands was the combined emission from more than one fluorophore. Current efforts by our group to further develop the multispectral FLIM endoscopy design include: the use of dual wavelength excitation and narrower emission spectral bands to enable more specific interrogation of collagen, NADH, FAD and porphyrin autofluorescence; the adoption of a novel frequency-domain FLIM implementation to significantly reduce endoscopy instrumentation complexity and cost [36]; and the addition of structured illumination based optical sectioning to enable more specific epithelial interrogation [37]. The statistical analyses applied to the quantified multispectral FLIM endoscopy based autofluorescence biomarkers showed their promising potential to differentiate between precancerous/cancerous from healthy oral epithelial tissue. However, these encouraging preliminary results need to be further validated. Current efforts by our group aim to thoroughly assess the capabilities of endogenous multispectral FLIM endoscopy as an image-guided surgical tool for detecting positive margins during head and neck cancer resection surgery.

2.5 Conclusions

This study represents, to the best of our knowledge, the first demonstration of label-free biochemical and metabolic clinical imaging of precancerous and cancerous oral lesions by means of widefield multispectral autofluorescence lifetime endoscopy. Moreover, a number of both established and potentially new autofluorescence biochemical and metabolic biomarkers of oral epithelial dysplasia and SCC were successfully imaged and quantified. This first-of-a-kind study has demonstrated the capabilities of endogenous multispectral FLIM endoscopy in differentiating precancerous/cancerous oral lesions from healthy oral tissue. Future studies will assess the capa-

bilities of endogenous multispectral FLIM endoscopy as an image-guided surgical tool for rapidly and accurately determining margin involvement during head and neck cancer resection surgery.

3. CAD SYSTEM FOR AUTOMATED DETECTION OF PRE-CANCEROUS AND CANCEROUS ORAL LESIONS VS. HEALTHY ORAL TISSUE BASED ON MULTISPECTRAL AUTOFLUORESCENCE ENDOSCOPY

3.1 Introduction

Several optical imaging technologies have been evaluated for the identification of positive surgical margins. Grillone et al. performed an in vivo study on 34 patients, in which elastic scattering spectroscopy (ESS) and a machine learning diagnostic algorithm were used to distinguish normal from abnormal oral tissue (mild/moderate/severe dysplasia, carcinoma in situ, and invasive cancer). This method achieved levels of sensitivity ranging from 84% to100% and specificity ranging from 71% to 89%, depending on how the cutoff between normal and abnormal tissue was defined (i.e., mild, moderate, or severe dysplasia) [38]. In an ex vivo study, Hamdoon et al. used optical coherence tomography (OCT) to scan tumor margins from 28 oral squamous cell carcinoma (OSCC) patients following resection, and differentiated tumor-free from tumor-involved margins with levels of sensitivity and specificity of 81.5% and 87%, respectively [39]. Jeng et al. used Raman spectroscopy (RS) in an ex vivo study to image 44 tumor and 36 normal oral tissue samples from patients and implemented a quadratic discriminant analysis (QDA) classifier to distinguish tumor from normal oral tissue, resulting in levels of sensitivity and specificity of $\sim$91% and $\sim$83%, respectively [40]. Fei et al. performed ex vivo hyperspectral imaging (HSI) on 20 patients and discriminated SCC margins from normal oral tissue with 84% sensitivity and 74% specificity using a convolutional neural network (CNN) classifier. Nayak et al. performed ex vivo autofluorescence spectroscopy (AFS) of normal, premalignant, and malignant oral tissues from patients and designed an artificial neural network (ANN) that displayed levels of sensitivity and specificity of 96.5% and 100%, respectively [41]. In an in vivo study, Huang et al. used a two-channel autofluorescence device targeting NADH and FAD autofluorescence to classify 49 cancerous lesions, 34 precancerous lesions, and 77 healthy oral mucosa from patients. They reported that precancerous

and cancerous lesions were differentiated from healthy oral mucosa with a sensitivity of $\sim$92% and specificity of $\sim$75% [22].

The encouraging results reported in these studies demonstrate capability in discriminating precancerous and cancerous oral lesions from healthy oral tissue. However, further studies are needed to translate these optical technologies to the clinic. In this study, we hypothesized that widefield multispectral autofluorescence-derived features quantified with our autofluorescence endoscopy system [26] can be used to develop a computational framework for a computer aided detection (CAD) system for the automated discrimination of cancerous and precancerous oral lesions from healthy oral tissue.

3.2 Methods

3.2.1 Multispectral Autofluorescence Image Database

The database used in this study included in vivo clinical endogenous multispectral autofluorescence images of 35 cancerous (SCC) and 5 precancerous (3 moderate dysplastic, MOD-DYS; 2 high-grade dysplastic, HG-DYS) oral lesions from 39 patients previously acquired following the imaging protocol described in **subsection 2.2.1**. These images were used to design and validate a computational framework for automated cancerous/precancerous vs. normal classification.

In a second autofluorescence endoscopic imaging phase, nine oral lesions (8 SCC; 1 HG-DYS) and corresponding contralateral normal oral tissues from nine patients were imaged and used exclusively to test the proposed computational framework

3.2.2 Multispectral Autofluorescence Feature Computation

For each pixel within the FOV of the lesion's autofluorescence image, nine multispectral features were computed as follows. The absolute fluorescence intensity measured at each emission band $I_\lambda(x, y)$ was computed per pixel (x, y) using **Equation 2.1**. The multispectral normalized fluorescence intensity $I_{\lambda,n}(x, y)$ was computed from the multispectral absolute fluorescence intensities $I_\lambda(x, y)$ using **Equation 2.2**. Finally, six ratios between multispectral absolute fluorescence intensities were computed, resulting in a total of nine autofluorescence-derived features computed

	Autofluorescence Feature
Multispectral Normalized Fluorescence Intensity	$I_{390,n}(x,y)$
	$I_{452,n}(x,y)$
	$I_{500,n}(x,y)$
Multispectral Absolute Fluorescence Intensity Ratio	$I_{390,n}(x,y)/I_{452,n}(x,y)$
	$I_{390,n}(x,y)/I_{500,n}(x,y)$
	$I_{452,n}(x,y)/I_{500,n}(x,y)$
	$[I_{452,n}(x,y)+I_{500,n}(x,y)]/I_{390,n}(x,y)$
	$[I_{390,n}(x,y)+I_{500,n}(x,y)]/I_{452,n}(x,y)$
	$[I_{390,n}(x,y)+I_{452,n}(x,y)]/I_{500,n}(x,y)$
Total Number	**9**

Table 3.1: Summary of multispectral autofluorescence features computed per pixel.

per image pixel, as summarized in Table 3.1.

3.2.3 Image Classification and Performance Estimation

In order to identify an optimal computational framework for the CAD system, the dataset of 40 multiparametric spectral autofluorescence images of oral lesions and 40 paired contralateral normal images was analyzed following the computational workflow summarized in Figure 3.1. First, the dataset was divided in training and validation sets following a leave-one-out-cross-validation (LOOCV) strategy, and the number of features was reduced using a correlation-based feature selection approach [42]. Second, the training samples (n = 79) entered a sequential forward search feature selection (up to 3 features) and classifier training stage using a second LOOCV method. Within this feature selection stage, a threshold of 50% on the pixel-level classifier posterior probability was applied to generate binary classification maps. Receiver Operating Characteristic (ROC) analysis was performed on the image-level percentage of positive pixels within each classification map and the optimal feature set was identified based on the ROC area under the curve (AUC). Third, the classifier was retrained using all training samples and binary classification maps were generated after applying a 50% threshold on the pixel-level posterior probability. To classify each complete classification map as either POSITIVE or NEGATIVE, an image-level threshold on the percentage of positive pixels was optimized by selecting the closest point to the upper left corner on

the ROC curve. The trained classifier was then applied, together with the 50% pixel-level threshold and the image-level threshold, to the testing sample. Finally, the whole process was repeated within the main LOOCV loop until every image in the dataset was used as a testing sample.

Six classifiers were evaluated in the computational framework shown in Figure 3.1: Linear (LDA), Diagonal-Linear (DLDA), Quadratic (QDA), Diagonal-Quadratic (DQDA) Discriminants, Support Vector Machines (SVM), and Logistic Regression (LOGREG).

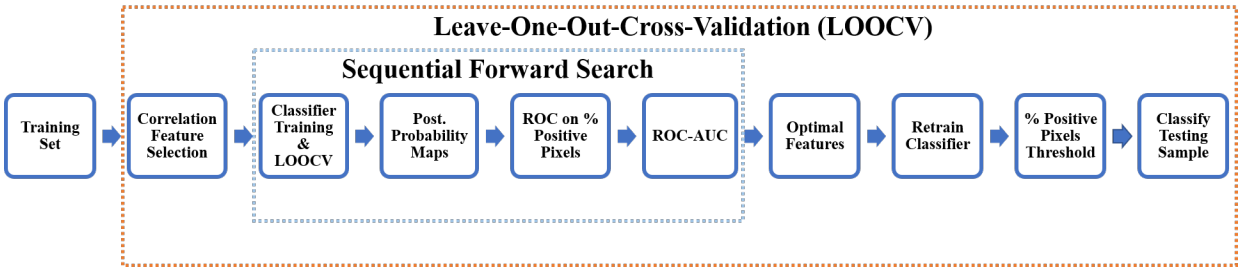

Figure 3.1: Computational framework for the CAD system.

3.3 Results

The classification performance on the training dataset obtained for each of the six classifiers evaluated is presented in Figure 3.2. The DQDA classifier yielded the highest accuracy ($\sim$84%) and levels of sensitivity and specificity of 85% and 83%, respectively.

The most frequently selected feature set identified in the workflow from Figure 3.1 consisted in the following autofluorescence spectral features:

1. The normalized fluorescence intensity in channel > 500 nm, $I_{500,n}(x, y)$, manily associated to FAD autofluorescence.

2. The absolute fluorescence intensity of channels 452 $\pm$ 22.5 nm and > 500 nm, relative to 390 $\pm$ 20 nm, $[I_{452}(x, y) + I_{500}(x, y)]/I_{390}(x, y)$, which quantifies the autofluorescence of NADH and FAD relative to collagen, respectively.

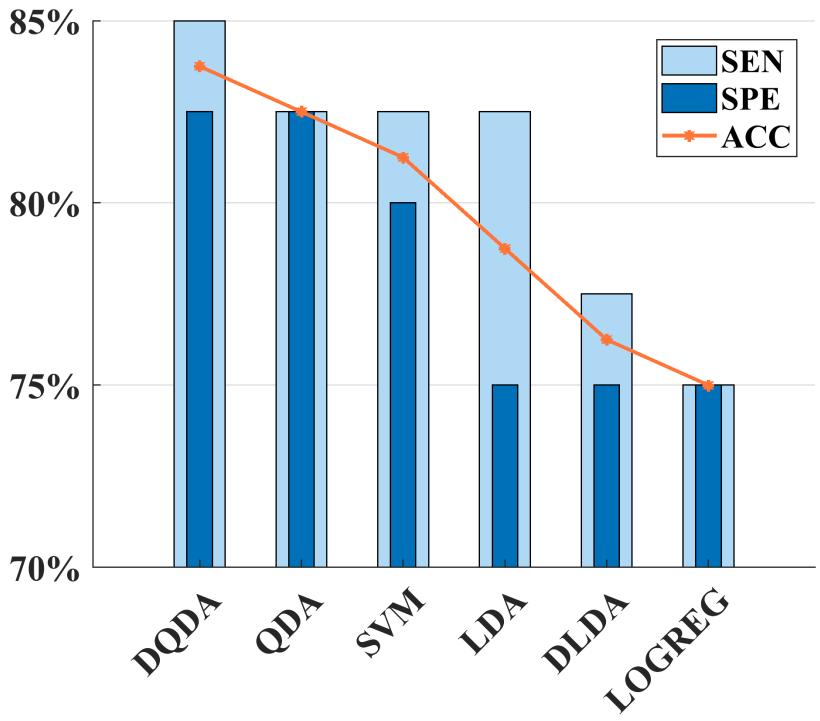

Figure 3.2: Classifier training performance. SEN: Sensitivity; SPE: Specificity; ACC: Accuracy.

The DQDA classifier was retrained using the complete training dataset (n = 80) and most relevant spectral features ($I_{500,n}$, $[I_{452} + I_{500}]/I_{390}$), yielding an optimal decision boundary that successfully discriminated SCC/HG-DYS/MOD-DYS from normal (Figure 3.3). An optimized image-level threshold of 28% on the percentage of positive pixels was selected based on the closest point to the upper left corner on the ROC curve. The optimal DQDA classifier, together with the 50% pixel-level and 28% image-level thresholds, was applied to the independent testing dataset (n = 18). The resulting DQDA posterior probability maps of the nine oral lesions and paired normal oral tissues used for testing are presented in Figure 3.4A. In these maps, each pixel represents a probability of belonging to the cancer/precancer (SCC/HG-DYS/MOD-DYS) class. The predicted image-level binary classification (POSITIVE/NEGATIVE) was obtained by first applying the 50% pixel-level probability threshold, yielding the classification maps presented in Figure 3.4B, and then applying the 28% image-level threshold on the percentage of positive pixels.

The confusion matrix resulting from the testing dataset classification is presented in Table 3.2.

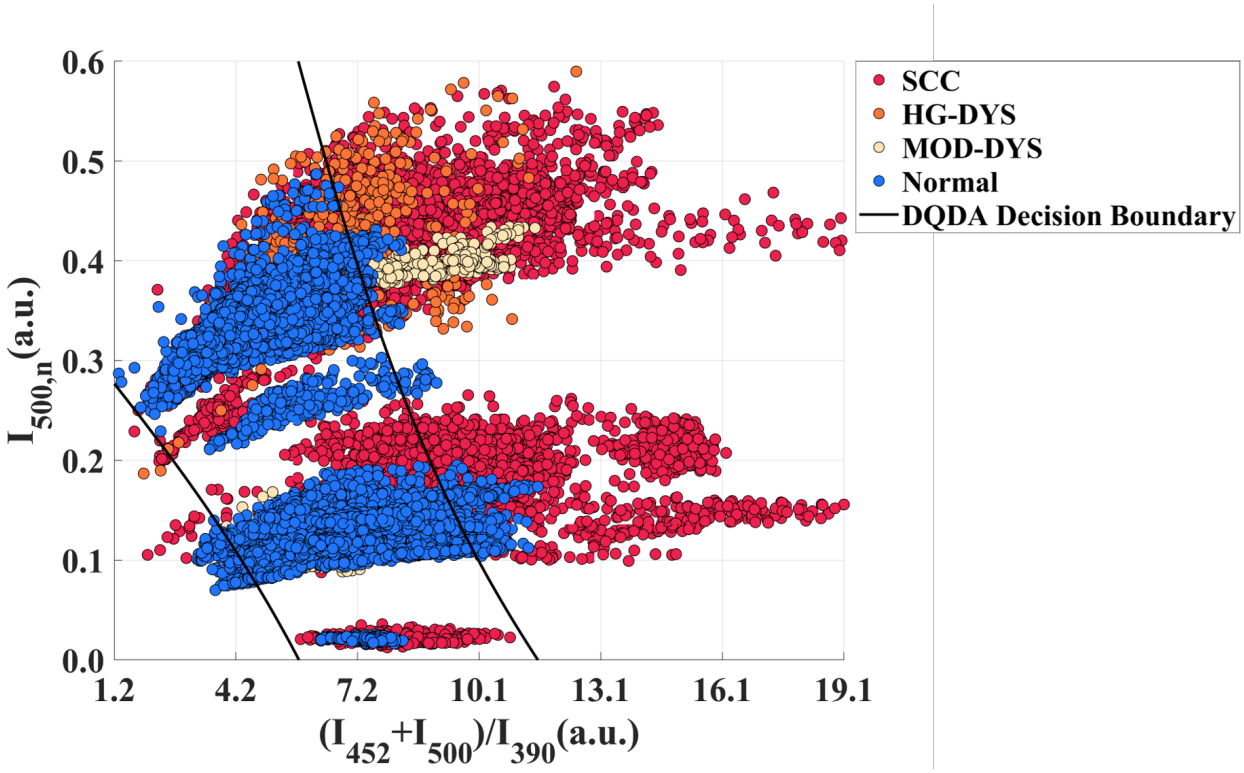

Figure 3.3: Optimal DQDA decision boundary obtained with the training dataset.

The image-level classification predicted by the optimized DQDA classifier is compared against the histopathological classification (gold standard). The DQDA classifier displayed levels of sensitivity and specificity of 78% and 100%, respectively; positive and negative predictive values (PPV, NPV) of 100% and 82%, respectively; and overall accuracy of 89%.

3.4 Discussion

In vivo multispectral autofluorescence endoscopy using a single 355 nm excitation wavelength was performed in this study for the clinical imaging of cancerous and precancerous oral lesions from 48 patients. The acquired endoscopic autofluorescence images were processed to generate multiparametric spectral autofluorescence images that were introduced into a computational framework for automated classification. In this computational framework, 40 oral lesion images paired with normal oral tissues were used for classifier training, and a systematic selection of the best spectral feature combination was performed to optimize a DQDA classifier for the discrimination

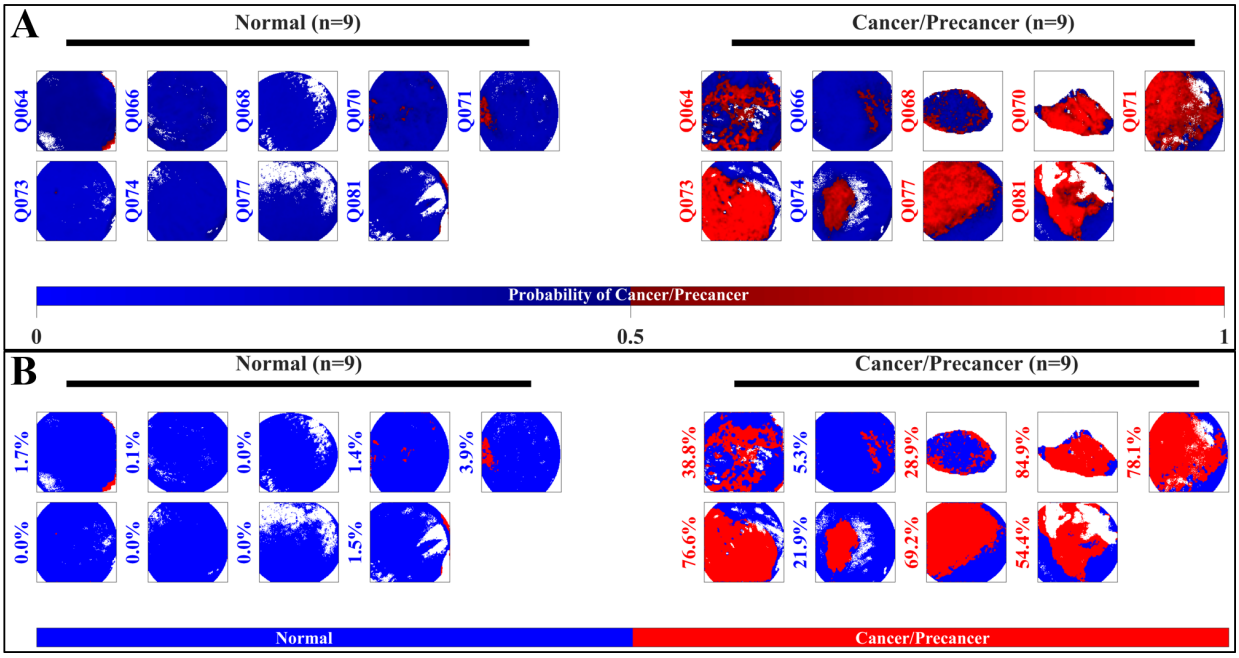

Figure 3.4: Posterior probability maps of nine cancerous/precancerous oral lesions and paired normal oral tissues (A). Patient identification numbers are shown on the left of each map and color-coded red if positive and blue if negative according to the predicted image-level classification. Corresponding classification maps of these oral lesions and normal tissues are also presented (B). Percentages of positive pixels are shown on the left of each classification map.

of cancerous/precancerous vs. normal oral tissue. The optimized DQDA classifier was tested on an independent dataset consisting of nine oral lesion images and the classification performance displayed levels of sensitivity and specificity of 78% and 100%, respectively.

The DQDA posterior probability maps of the nine imaged oral lesions used for testing (Figure 3.4A) indicate the pixel-level likelihood of malignancy and display evident contrast between cancerous/precancerous and normal oral tissues. The application of a threshold at 50% on the pixel posterior probabilities enabled the generation of binary classification maps (Figure 3.4B) from which the classification of the whole image was predicted based on the optimized image-level threshold at 28% applied on the percentage of positive pixels. The optimized DQDA classifier was able to successfully predict 9/9 normal, 6/8 cancerous (SCC), and 1/1 precancerous (HG-DYS) oral tissue images as indicated in Table 3.2. The two misclassified cancerous (SCC) cases are likely due to the small size of the imaged oral lesion relative to its FOV, since small regions of red-colored pix-

		Predicted		
		Normal	**HG-DYS/SCC**	**Total**
True	**Normal**	9	0	9
	HG-DYS	0	1	1
	SCC	2	6	8
	Total	11	7	18

Table 3.2: Confusion matrix of the testing dataset classification. HG-DYS: High-Grade Dysplasia, SCC: Squamous Cell Carcinoma.

Optical Modality	Number of Patients	Classification Task	Classification Performance	Reference
AFI (VELscope®)	58	CAN vs. PRE vs. NOR	ROC-AUC = 0.87-0.95	[43]
AFI	141	CAN vs. NOR	SEN/SPE = 71%-98%/91%-100%	[44]
		PRE vs. NOR	SEN/SPE = 92%-94%/86%-100%	
AFI	160	PRE/CAN vs. NOR	SEN/SPE = 92%/75%	[22]
AFI (VELscope®)	140	CAN vs. NOR	SEN/SPE = 98%/92%	[45]
		PRE/CAN vs. NOR	SEN/SPE = 97%/92%	
AFS	251	CAN vs. NOR	ROC-AUC = 0.97	[46]

Table 3.3: Summary of in vivo autofluorescence spectroscopy and imaging studies. AFI: Autofluorescence Imaging, AFS: Autofluorescence Spectroscopy, CAN: Cancer, PRE: Precancer, NOR: Normal, SEN: Sensitivity, SPE: Specificity, ROC-AUC: Receiver Operating Characteristic Area Under Curve.

els are observed in the posterior probability maps (Figure 3.4A) of the missed positive cases (Q066 and Q074), resulting in percentages of positive pixels below the selected image-level threshold of 28%, as indicated in the classification maps (Figure 3.4B). Nevertheless, these classification maps can be clinically relevant for a more accurate demarcation of the extension of the malignant oral lesion, since the observed red-colored area clearly indicate its potential location within the imaged FOV. Therefore, this novel autofluorescence-based CAD tool results promising for aiding doctors during the surgical resection of cancerous and precancerous oral epithelial lesions from patients.

Several in vivo autofluorescence spectroscopy (AFS) and imaging (AFI) human studies have investigated the systematic discrimination of cancerous and precancerous oral lesions from normal oral tissue. The most relevant studies reported to date are summarized in Table 3.3.

Jeng et al. performed AFI in 58 patients using the VELscope®, which is a commercially available autofluorescence tool for oral cancer screening developed by Apteryx Imaging. They

reported the successful discrimination between cancerous, precancerous, and normal oral tissue with a ROC-AUC ranging from 0.87 to 0.95 [43]. Nevertheless, their study only classified tongue and buccal mucosa lesions independently and no optimal ROC threshold was reported to enable comparison of the levels of sensitivity and specificity. Our study has the advantage of combining cancerous and precancerous oral lesions from different anatomical sites as indicated in Table 2.1, resulting in a more clinically relevant classification approach that is robust to oral tissue autofluorescence variability due to lesion anatomical location. In another study, Kumar et al. used AFI in 141 patients and reported sensitivity and specificity of 71%-98% and 91%-100%, respectively in cancerous vs. normal oral tissue classification, and 92%-94% sensitivity and 86%-100% specificity in precancerous vs. normal oral tissue classification [44]. However, these promising classification results were obtained by separately classifying buccal mucosa, lateral border of tongue, and dorsal surface of tongue tissues, which likely facilitated the discrimination between cancerous/precancerous and normal oral tissue due to the homogeneity of the imaged lesion sites. In addition, their imaging system only interrogated the endogenous autofluorescence of FAD and porphyrins. Our system not only interrogated the autofluorescence of FAD, but also that of connective tissue collagen and NADH. In particular, the spectral information obtained at the collagen (390 ± 20 nm) and FAD (> 500 nm) emission channels was relevant to successfully discriminate cancerous/precancerous lesions from healthy oral tissue, since the ratio $[I_{452} + I_{500}]/I_{390}$, which quantifies the autofluorescence of NADH (I_{452}) and FAD (I_{500}) relative to collagen (I_{390}), and the normalized intensity in channel > 500 nm ($I_{500,n}$) resulted in the most powerful features for classification (Figure 3.3). Therefore, the simultaneous autofluorescence imaging of collagen, NADH, and FAD performed with our multispectral endoscopy system provided relevant morphological and metabolic information that enabled contrast between malignant and normal oral tissue. Huang et al. performed AFI in 160 patients using a two-channel autofluorescence device to differentiate precancerous and cancerous lesions from normal oral tissue with sensitivity of 92% and specificity of 75% [22]. Nonetheless, the classification performance reported in their study was based on randomly selected samples from a training dataset used to design a QDA classifier; thus, not per-

forming any validation on an independent pool of data. In contrast, our optimized DQDA classifier was validated using a dataset of nine oral lesions and contralateral normal oral tissues completely blinded to the classifier training and optimization stage, resulting in an unbiased and more accurate estimation of the classification performance. In another related study, Huang et al. performed AFI in 140 patients using the VELscope® and reported sensitivity and specificity of 98% and 92%, respectively in cancerous vs. normal oral tissue, and 98% sensitivity and 92% specificity in cancerous/precancerous vs. normal oral tissue [45]. However, the classification performance reported in their study was based solely on training data and no classifier validation was performed on an independent dataset, which would have more clinical relevance. Finally, de Veld et al. performed AFS in 251 patients and reported a ROC-AUC of 0.97 in cancerous vs. normal oral tissue [46]. Unfortunately, a comparison in terms of sensitivity and specificity cannot be made since they did not report the selection of a specific ROC threshold for classification. Moreover, six excitation wavelengths in the range of 365 nm – 450 nm were used in their study to record the autofluorescence spectra of oral lesions. Here we performed multispectral autofluorescence endoscopy imaging of oral lesions using a single 355 nm excitation wavelength, which results in a much simpler and less costly clinically compatible system.

3.4.1 Study Limitations

The application of a fixed image-level threshold on the percentage of positive pixels to predict the image classification label could result in misclassification of small oral epithelial lesions as observed in the classification maps of two positive cases (Q066 and Q074, Figure 3.4B). Therefore, a more diverse training dataset with a variety of oral lesions of different sizes should be included in further studies to perform a better systematic selection of the image-level threshold, which could potentially reduce the number of missed positive cases. Moreover, the limited sample size of the testing dataset used in this study results in >10% reduction in the levels of sensitivity and/or specificity for each missed positive and/or negative case. Hence, a larger validation dataset is needed to obtain a better estimation of the classification performance.

In summary, this in vivo study in humans demonstrates the capabilities of widefield multispec-

tral autofluorescence endoscopy in providing contrast between cancerous/precancerous oral lesions and normal oral tissue with clinically relevant levels of sensitivity and specificity. The limited sample size used in this study, however, raises the need to further develop and clinically validate the proposed computational framework for the CAD system. Once fully developed and validated, this novel diagnostic tool could potentially aid oral pathologists during the clinical identification of surgical resection margins.

3.5 Conclusions

In vivo widefield multispectral autofluorescence endoscopy was used for the clinical imaging of cancerous and precancerous oral lesions from patients. The outcomes of this study demonstrate the potentials of a CAD system based on multispectral autofluorescence endoscopy as a clinical tool for automated, non-invasive and in situ identification of cancerous/precancerous oral lesions from healthy oral tissue. Once fully validated clinically, this tool will facilitate the identification of positive surgical margins during conventional clinical examination of oral epithelial lesions.

4. MULTISPECTRAL FLUORESCENCE LIFETIME ENDOSCOPIC IMAGING OF BENIGN, DYSPLASTIC, AND CANCEROUS ORAL LESIONS

4.1 Introduction

Oral cancer patients who are diagnosed at advanced stages commonly require complex and highly invasive surgery and have a five-year survival rate of only 39%, while patients who are diagnosed at early stages usually require minor surgery and have an 84% chance of survival [1]. Unfortunately, benign oral lesions are often difficult to distinguish from dysplastic lesions and oral squamous cell carcinoma (OSCC) [47, 48]. As a result, only three in ten patients are diagnosed at early stages [1]. The current gold standard for the diagnosis of OSCC and dysplasia is conventional oral examination followed by tissue biopsy and histopathological analysis of clinically suspicious oral lesions [49]. However, this procedure has several limitations, such as underdiagnosis or misdiagnosis resulting from sampling bias, training of both a clinician and pathologist, lengthy time to diagnosis, subjective grading of dysplastic lesions, and patient morbidity and discomfort due to invasive surgery [49]. Therefore, fast and accurate tools for oral cancer and precancer screening are urgently needed to improve the survival rate and quality of life of these patients, while reducing the number of unnecessary tissue biopsies of benign oral lesions.

Several commercially available diagnostic adjuncts have been developed to assist with the clinical evaluation of potentially malignant and premalignant oral lesions: Toluidine blue, brush cytology, acetowhitening with chemiluminescence (ViziLite), and autofluorescence imaging (VELscope, Identafi, and OralID). Nevertheless, these diagnostic adjuncts have low specificity and are not generally recommended for the assessment of clinically suspicious oral lesions [49, 50].

Several studies have explored the use of autofluorescence spectroscopy (AFS), time-resolved fluorescence spectroscopy (TRFS), confocal fluorescence microscopy (CFM), and fluorescence lifetime imaging microscopy (FLIM) to identify optical biomarkers of oral SCC and dysplasia. In an in vivo study in 38 patients, Wang et al. used TRFS at the 633 nm wavelength to differentiate

dysplastic vs. benign (verrucous hyperplasia and epithelial hyperplasia) lesions with a sensitivity of 93% and specificity of 75% [51]. In an ex vivo study using CFM in human oral biopsies, Gillenwater et al. reported increased epithelial and decreased connective tissue autofluorescence in dysplasia relative to benign inflammation upon ultraviolet excitation [20]. Krishnakumar et al. performed ex vivo AFS in hamsters and reported decreased autofluorescence intensity at the 380 nm emission wavelength and decreased redox ratio in dysplasia and well-differentiated squamous cell carcinoma (WDSCC) relative to benign (hyperplasia) [33]. Our group previously performed in vivo multispectral FLIM in hamsters and reported lower normalized intensity and shorter average lifetime at the 390 $\pm$ 20 nm band, shorter average lifetime at the 450 $\pm$ 22.5 nm band, and higher normalized intensity at the >500 nm band in high-grade dysplastic/carcinoma vs. benign oral lesions [52]. Even though these studies have provided promising results, none of these imaging tools have been translated yet to the clinic for aiding in the discrimination of cancerous/precancerous from benign oral lesions.

In this study, we hypothesized that widefield multispectral FLIM endoscopy imaging of clinically suspicious oral lesions can provide novel autofluorescence biomarkers of oral dysplasia and SCC useful for the discrimination of cancerous and precancerous oral lesions from benign oral tissue.

4.2 Methods

4.2.1 FLIM Instrumentation and Clinical Imaging of Oral Lesions

Clinical endogenous multispectral FLIM images of benign, dysplastic and cancerous oral lesions from 118 patients were acquired in vivo following the study protocol described in **subsection 2.2.1**. The distribution of the 124 imaged oral lesions, based in both anatomical location and histopathological diagnosis, is provided in Table 4.1

4.2.2 Multispectral FLIM Feature Computation

The acquired multispectral endoscopic FLIM images were processed following the methodology described in **subsection 2.2.2**, yielding 16 FLIM-derived features per image pixel. In addition,

Lesion Location	Histopathology Diagnosis				Total Number
	Benign	MOD-DYS	HG-DYS	SCC	
Buccal Mucosa	29	2	1	11	**43**
Tongue	21	1	0	12	**34**
Gingiva	17	0	1	7	**25**
Lip	5	0	0	2	**7**
Mandible	4	0	0	1	**5**
Palate	4	0	0	0	**4**
Floor of Mouth	3	0	0	1	**4**
Maxilla	1	0	0	1	**2**
Total Number	**84**	**3**	**2**	**35**	**124**

Table 4.1: Distribution of the 124 imaged oral lesions based in both anatomical location and histopathological diagnosis (MOD-DYS: Moderate Dysplasia; HG-DYS: High-Grade Dysplasia; SCC: Squamous Cell Carcinoma).

feature relative values $^{\Delta}f(x,y)$ were computed per pixel by taking the difference between each pixel feature value $f(x,y)$ within the FOV of the lesion's autofluorescence image and the median feature value of the FOV of the paired contralateral (Normal) image $\mu_{f,Normal}$ for each of the 16 FLIM-derived parameters:

$$^{\Delta}f(x,y) = f(x,y) - \mu_{f,Normal} \tag{4.1}$$

Therefore, a total of 32 multispectral FLIM-derived features were computed at each spatial location (x,y) within the FOV of the oral lesion's autofluorescence image. These features are categorized as follows: 1) Normalized autofluorescence intensities, 2) Bi-exponential decay parameters, 3) Average fluorescence lifetimes, 4) Redox Ratio, and 5) Relative values. A list of the FLIM-derived features included within these categories is presented in Table 4.2.

4.2.3 Statistical Analysis of Multispectral FLIM Features

As summarized in Table 4.1, the 124 imaged oral lesions corresponded to 84 benign, 5 precancerous (3 MOD-DYS, 2 HG-DYS), and 35 cancerous (SCC) lesions. In order to identify statistical differences in the distribution mean of each of the 32 FLIM features presented in Table 4.2 from precancerous or cancerous oral tissue versus benign oral tissue, the following statistical analysis was performed. For each imaged oral tissue region, multi-parametric FLIM maps were generated,

Feature Category	Spectral Band			Total Number
	390 ± 20 nm	**452 ± 22.5 nm**	**>500 nm**	
Normalized Autofluorescence Intensity	$I_{390,n}(x,y)$	$I_{452,n}(x,y)$	$I_{500,n}(x,y)$	**3**
Bi-Exponential Decay Parameters	$\tau_{fast,390}(x,y)$	$\tau_{fast,452}(x,y)$	$\tau_{fast,500}(x,y)$	**9**
	$\tau_{slow,390}(x,y)$	$\tau_{slow,452}(x,y)$	$\tau_{slow,500}(x,y)$	
	$\alpha_{fast,390}(x,y)$	$\alpha_{fast,452}(x,y)$	$\alpha_{fast,500}(x,y)$	
Average Fluorescence Lifetime	$\tau_{avg,390}(x,y)$	$\tau_{avg,452}(x,y)$	$\tau_{avg,500}(x,y)$	**3**
Redox Ratio	$I_{452}(x,y)/I_{500}(x,y)$			**1**
Relative Values	$^{\Delta}f(x,y)$			**16**
Total Number				**32**

Table 4.2: Summary of FLIM-derived features computed per pixel for each spectral band.

in which the 32 FLIM features were computed at each image pixel. Then, for each FLIM feature map, the median feature value from all pixels was computed; thus, each imaged oral tissue region was represented by a single feature vector composed of the median values of each of the 32 FLIM feature maps. Finally, a two-tailed Mann-Whitney U test was applied to the precancerous/cancerous vs. benign median values of each of the 32 FLIM features, with a type-1 error probability of $p<0.05$ for all tests.

4.3 Results

The statistical analysis performed on the autofluorescence feature median value distributions revealed that the distribution means of 13 FLIM features were statistically significantly different ($P < 0.05$) in moderate and high-grade dysplastic/SCC (n = 40) vs. benign (n = 84) oral lesions. Box plots of the feature median value distributions from each group are shown in Figure 4.1

Representative FLIM feature maps comparing cancerous (SCC) floor of mouth tissue and benign tongue tissue from two patients are presented in Figure 4.2, and FLIM feature maps comparing precancerous (HG-DYS) and benign buccal mucosal tissue from two patients are shown in Figure 4.3. In both representative cases, the pixel distributions of each FLIM feature map were consistent with the observed trends in the distribution mean of each of the 13 statistically different FLIM features from moderate and high-grade dysplastic/cancerous versus benign oral lesions.

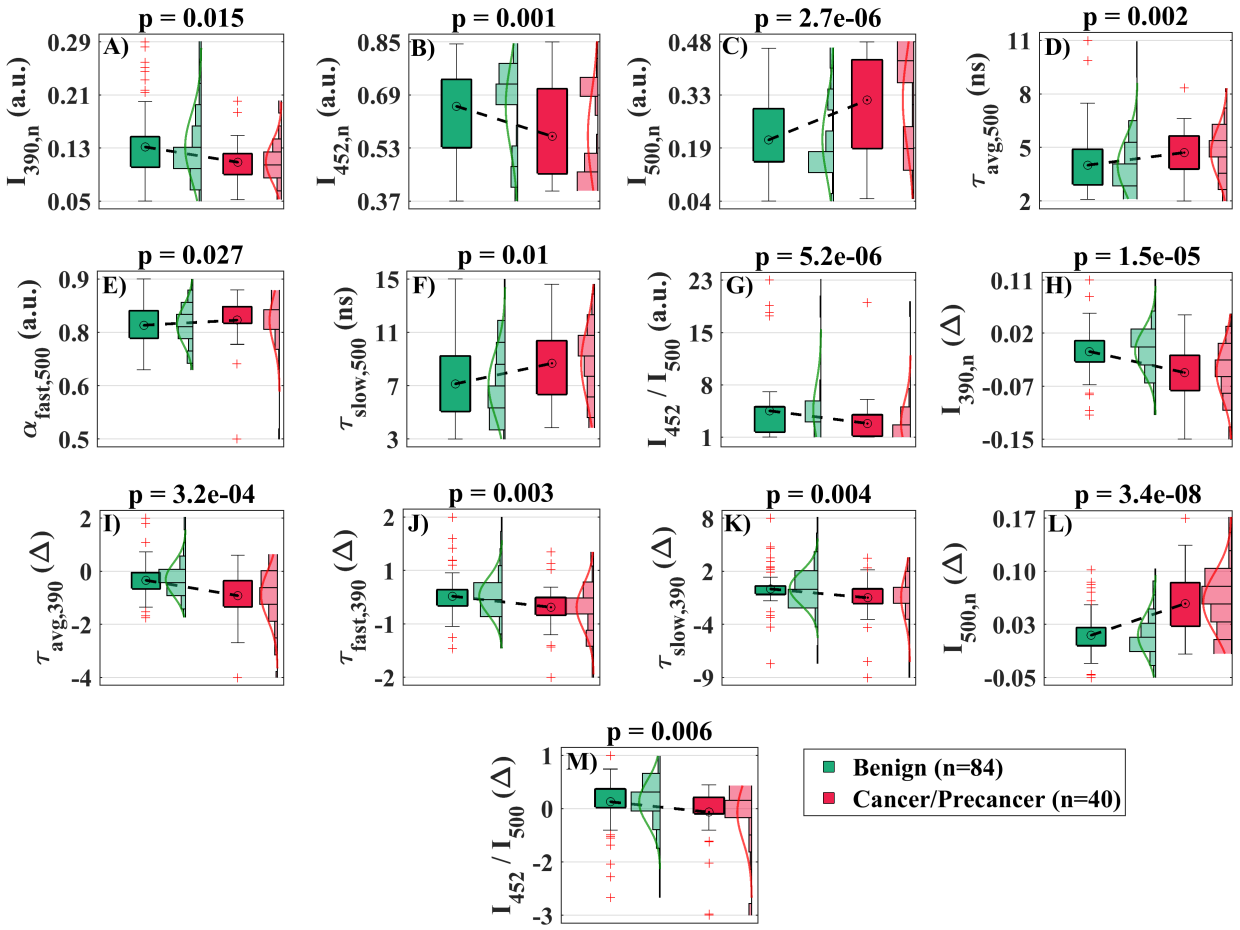

Figure 4.1: Box plots of FLIM-derived feature median value distributions of benign (n=84; green boxes), moderate dysplastic (MOD-DYS), high-grade dysplastic (HG-DYS), and cancerous (SCC) oral lesions (n=40; red boxes). Feature median value distributions for each group are also shown. P-values resulting from two-tailed Mann-Whitney U tests are presented on top of each plot. Δ: Relative values.

4.4 Discussion

In this study, in vivo multispectral FLIM endoscopic clinical imaging of benign, precancerous, and cancerous oral lesions from 118 patients was performed quickly (<3 s per image) and non-invasively. The acquired multispectral FLIM endoscopic images were processed to generate widefield maps of absolute and relative autofluorescence spectral and lifetime features of benign and precancerous/cancerous oral lesions. The statistical analysis applied to each of these autofluorescence feature maps identified several ones (Figure 4.1) that displayed statistically significant

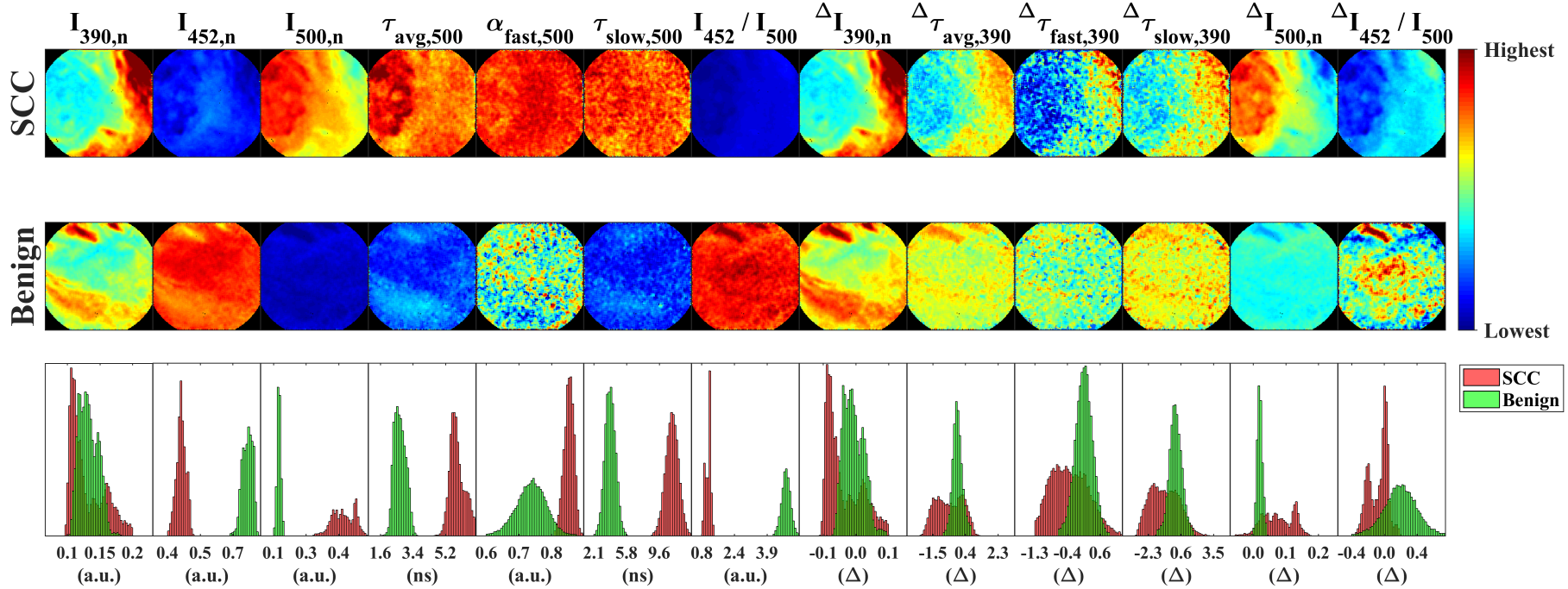

Figure 4.2: Multispectral FLIM feature maps of cancerous (SCC; top panels) floor of mouth tissue and benign (middle panels) tongue tissue from two patients. Pixel distributions of benign and SCC maps for each feature are also compared (bottom panels). The trends observed in this representative case are consistent with the statistical findings on the feature image median value distributions from precancerous/cancerous vs. benign oral tissue. Δ: Relative values.

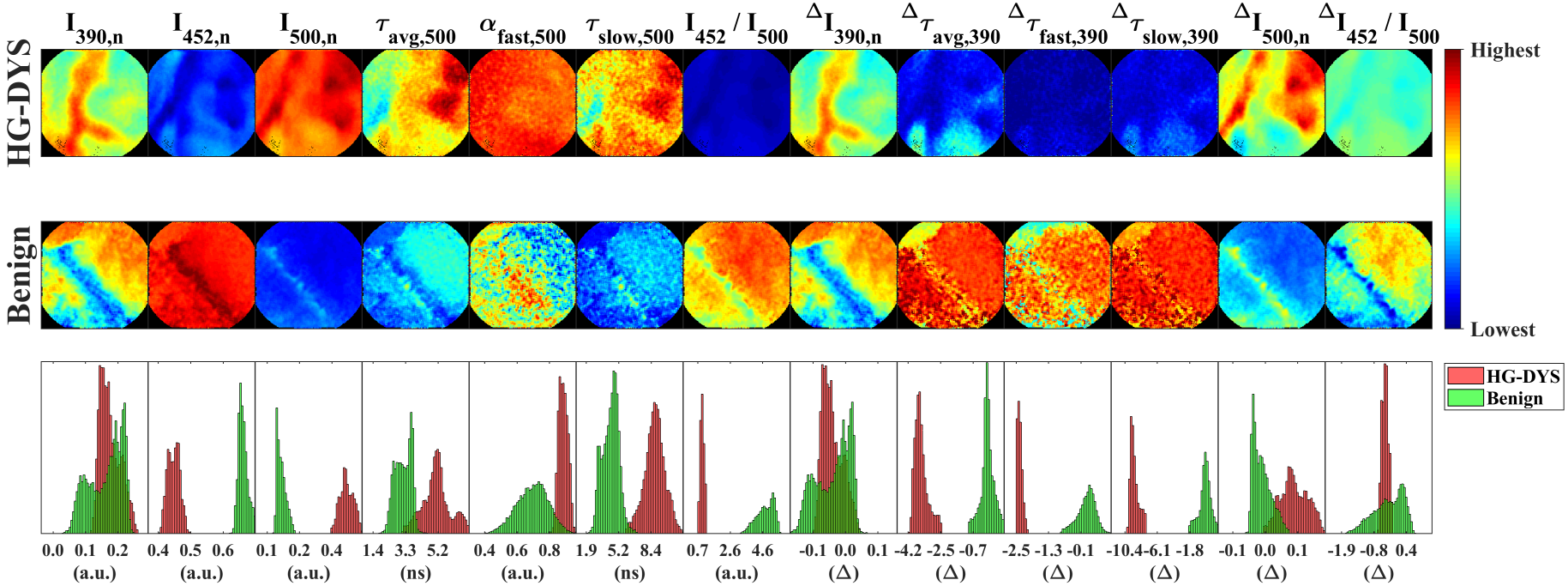

Figure 4.3: Multispectral FLIM feature maps of precancerous (HG-DYS; top panels) and benign (middle panels) buccal mucosal tissue from two patients. Pixel distributions of benign and HG-DYS maps for each feature are also compared (bottom panels). The trends observed in this representative case are consistent with the statistical findings on the feature image median value distributions from precancerous/cancerous vs. benign oral tissue. Δ: Relative values.

Emission Channel	Associated Fluorophore	FLIM-Derived Autofluorescence Features	Moderate and High-Grade Dysplasia / SCC vs. Benign	
			Observed Trend	Previous Studies [Ref.]
390 ± 20 nm	**Collagen**	$I_{390,n}$	↓	↓ Ex Vivo CFM: Humans [20] ↓ Ex Vivo AFS: Animals [33] ↓ In Vivo FLIM: Animals [49]
		${}^{\Delta}I_{390,n}$	↓	Not Reported
		${}^{\Delta}\tau_{avg,390}$	↓	Not Reported
		${}^{\Delta}\tau_{fast,390}$	↓	Not Reported
		${}^{\Delta}\tau_{slow,390}$	↓	Not Reported
452 ± 22.5 nm	**NADH**	$I_{452,n}$	↓	Not Reported
>500 nm	**FAD**	$I_{500,n}$	↑	↑ Ex Vivo CFM: Humans [20] ↑ In Vivo FLIM: Animals [49]
		${}^{\Delta}I_{500,n}$	↑	Not Reported
		$\tau_{avg,500}$	↑	Not Reported
		$\tau_{slow,500}$	↑	Not Reported
		$\alpha_{fast,500}$	↑	Not Reported
452 / 500 nm	**Redox-Ratio = NADH / FAD**	I_{452}/I_{500}	↓	↓ Ex Vivo AFS: Animals [33]
		${}^{\Delta}I_{452}/I_{500}$	↓	Not Reported

Table 4.3: Summary of trends in statistically different FLIM-derived features in Moderate and High-Grade Dysplasia/SCC vs. Benign. FLIM: Fluorescence Lifetime Imaging; AFS: Autofluorescence Spectroscopy; CFM: Confocal Fluorescence Microscopy.

differences between precancerous/cancerous vs. benign oral tissue. In Table 4.3, the statistical trends of the autofluorescence spectral and lifetime features observed in this study are summarized and compared to previously reported observations.

Significantly lower absolute ($I_{390,n}$, Figure 4.1A) and relative (${}^{\Delta}I_{390,n}$, Figure 4.1H) normalized autofluorescence intensities at the 390 ± 20 nm band in cancerous and precancerous oral lesions with respect to benign oral tissue were observed in this study. Because collagen in lamina propria is expected to be the main contributor to the oral epithelial tissue autofluorescence measured at this spectral band upon 355 nm excitation, the lower $I_{390,n}$ is likely due to the breakdown of collagen crosslinks in the connective tissue [19, 29] and the increase in both epithelial thickness and tissue optical scattering accompanying dysplastic or cancerous change [30]. Our finding is in agreement with previous observations [20, 33, 52]. In addition, we report what is, to the best of our knowledge, the first observation of a lower ${}^{\Delta}I_{390,n}$, which indicates that the normalized oral tissue autofluorescence at the 390 ± 20 nm band relative to the corresponding healthy oral tissue decreases more in precancerous/cancerous than in benign oral lesions. This endoscopic FLIM-derived feature could potentially represent a novel autofluorescence biomarker of oral cancer and dysplasia.

Our findings also indicated significantly shorter relative average ($^{\Delta}\tau_{avg,390}$, Figure 4.1I), fast-component ($^{\Delta}\tau_{fast,390}$, Figure 4.1J), and slow-component ($^{\Delta}\tau_{slow,390}$, Figure 4.1K) lifetimes at the 390 $\pm$ 20 nm emission spectral band in cancerous and precancerous oral lesions compared to benign oral tissue. To the best of our knowledge, this is the first observation of larger differences in autofluorescence lifetimes with the corresponding healthy oral tissue at the collagen emission peak in cancerous and precancerous oral lesions. Because of the overlap in the emission spectra of collagen and NADH at this spectral band, these observations are likely due to a larger decrease in the slower-decaying collagen signal in precancerous and cancerous oral lesions, resulting in overall faster tissue autofluorescence temporal response. Even though these FLIM-derived features could potentially become relevant autofluorescence biomarkers of oral cancer and dysplasia, further studies are needed to understand these observations.

Significantly lower absolute normalized autofluorescence intensity ($I_{452,n}$, Figure 4.1B) at the 452 $\pm$ 22.5 nm band was observed in cancerous and precancerous oral lesions with respect to benign oral tissue. To the best of our knowledge, this is the first observation of decreased oral epithelial autofluorescence at the NADH emission peak upon 355 nm excitation in precancerous/cancerous relative to benign oral lesions. Because of the overlap in the emission spectra of collagen and NADH at this spectral band, the much stronger decrease in collagen autofluorescence signal in cancerous/precancerous oral tissue might explain the observed lower $I_{452,n}$.

Significantly higher absolute ($I_{500,n}$, Figure 4.1C) and relative ($^{\Delta}I_{500,n}$, Figure 4.1L) normalized autofluorescence intensities at the > 500 nm band in cancerous and precancerous oral lesions compared to benign oral tissue were observed. The main contributor to the oral tissue autofluorescence measured at this spectral band upon 355 nm excitation is expected to be FAD within oral epithelial cells. Hence, the higher $I_{500,n}$, consistent with previous observations [20, 52], is likely due to oxidative phosphorylation, the most efficient cellular metabolic pathway that requires the oxidation of $FADH_2$ into FAD. Hence, the higher metabolic rate of malignant cells would result in increased levels of mitochondrial FAD [35]. The higher $^{\Delta}I_{500,n}$, which has not been previously observed, indicates that the normalized oral tissue autofluorescence at the > 500 nm band relative

to the corresponding healthy oral tissue increases more in precancerous/cancerous oral lesions than in benign oral tissue.

Our findings also indicated significantly longer average ($\tau_{avg,500}$, Figure 4.1D) and slow-component ($\tau_{slow,500}$, Figure 4.1F) lifetimes, and larger relative contribution of the fast-component lifetime ($\alpha_{fast,500}$, Figure 4.1E) at the > 500 nm spectral band in cancerous/precancerous relative to benign oral lesions. To the best of our knowledge, these observations have not been previously reported in cancerous/precancerous vs. benign human oral epithelial tissue. The larger $\tau_{avg,500}$ might be explained by a stronger contribution of FAD to the autofluorescence collected at this spectral channel, and the larger $\tau_{slow,500}$, associated to FAD lifetime, is likely to reflect increased levels of FAD in malignant oral epithelial cells [21]. Due to the single-photon 355 nm excitation and broad emission spectral band used in the FLIM endoscope, the tissue autofluorescence imaged at the > 500 nm spectral band could come not only from FAD but also from NADH. Therefore, the observed larger $\alpha_{fast,500}$ is likely due to increased contribution of NADH autofluorescence at this spectral band associated to the fast-component lifetime ($\tau_{fast,500}$).

Significantly lower absolute (I_{452}/I_{500}, Figure 4.1G) and relative ($^{\Delta}I_{452}/I_{500}$, Figure 4.1M) redox ratio were observed in precancerous and cancerous oral lesions with respect to benign oral tissue. Oxidative phosphorylation requires the oxidation of both NADH and $FADH_2$ molecules, resulting in a decreased NADH/FAD redox ratio [35]. Therefore, the observed lower I_{452}/I_{500} in cancerous and precancerous oral lesions, consistent with previous observations [33], could reflect increased cellular metabolic activity, a hallmark of epithelial cell malignant transformation [16]. The lower $^{\Delta}I_{452}/I_{500}$, which has not been previously observed, indicates that the redox ratio relative to the corresponding healthy oral tissue decreases more in precancerous/cancerous oral lesions compared to benign oral tissue.

Our three-channel multispectral FLIM endoscope, which acquired the autofluorescence mainly attributed to collagen, NADH, and FAD in oral epithelial tissue, enabled the computation of 13 FLIM-derived features that demonstrated contrast between cancerous/precancerous vs. benign oral lesions and were in agreement with previous observations from animals and humans. The relative

FLIM feature values, which contemplate the autofluorescence properties of the normal oral tissue, were relevant for the discrimination between malignant and benign oral lesions, suggesting that these types of lesions present unique autofluorescence signatures modulated by morphological and metabolic alterations relative to healthy oral tissue.

The statistically different trends in FLIM-derived features observed in this study have the potential to be relevant for the application of statistical classifiers for automated discrimination of cancerous/precancerous vs. benign oral lesions in a similar way performed by Wang et al. [51]. Their study reported the successful discrimination of precancerous vs. benign oral lesions from patients based on time-resolved autofluorescence of the endogenous fluorophore protoporphyrin IX (PpIX) acquired at 633 nm under 410 nm excitation. Encouraged by this study, subsequent research will focus on the use of machine learning strategies to systematically distinguish malignant/premalignant from benign oral lesions based on multispectral FLIM endoscopy. Moreover, the addition of a fourth spectral channel targeting PpIX to our current FLIM endoscopy system could potentially complement the acquired morphological and metabolic information due to collagen, NADH, and FAD autofluorescence, resulting in a more robust system for oral cancer and precancer screening.

4.4.1 Study Limitations

The multispectral FLIM endoscope used in this study was designed to preferentially interrogate the contributions of collagen, NADH and FAD in the oral tissue autofluorescence; however, it did not enable their specific interrogation due to the use of a single excitation wavelength and relatively broad emission spectral bands. Current efforts by our group to overcome this limitation include: the use of dual wavelength excitation and narrower emission spectral bands to enable more specific interrogation of collagen, NADH, FAD and porphyrin autofluorescence; and the adoption of a novel frequency-domain FLIM implementation to significantly reduce endoscopy instrumentation complexity and cost [36]. Moreover, the limited lateral resolution and lack of optical axial sectioning capabilities of the multispectral FLIM endoscope did not allow cellular resolution imaging of the epithelial layer independently from the submucosa. To overcome this

limitation, our group is currently evaluating the addition of structured illumination based optical sectioning to enable more specific epithelial interrogation [37].

The statistical analyses applied to the quantified multispectral FLIM endoscopy based autofluorescence biomarkers showed their promising potential to differentiate between cancerous/precancerous from benign oral epithelial tissue. However, these encouraging preliminary results need to be further validated. Current efforts by our group aim to thoroughly assess the capabilities of endogenous multispectral FLIM endoscopy as a CAD tool for discriminating cancerous/precancerous from benign oral tissue during clinical examination of potentially malignant oral lesions.

4.5 Conclusions

In this study, we performed label-free biochemical and metabolic clinical imaging of benign, precancerous and cancerous oral lesions by means of widefield multispectral autofluorescence lifetime endoscopy. Several potentially novel autofluorescence biomarkers of oral epithelial dysplasia and SCC useful for the discrimination of precancerous/cancerous oral lesions from benign oral tissue were identified. Future studies will assess the capabilities of endogenous multispectral FLIM endoscopy as a CAD tool for the fast and accurate discrimination of precancerous/cancerous from benign oral lesions during conventional oral examination.

5. CAD SYSTEM FOR AUTOMATED DETECTION OF PRE-CANCEROUS AND CANCEROUS ORAL LESIONS VS. BENIGN ORAL TISSUE BASED ON MULTISPECTRAL AUTOFLUORESCENCE IMAGING ENDOSCOPY

5.1 Introduction

Computational classification algorithms based on optical imaging technologies have been explored for the discrimination of precancerous and cancerous oral lesions vs. benign oral tissue. Guze et al. performed in vivo Raman spectroscopy (RS) in 18 patients to distinguish precancerous and cancerous oral lesions from benign and normal oral tissue [53]. This study reported levels of sensitivity and specificity of 100% and 77%, respectively. Ni et al. performed in vivo narrow band imaging (NBI) in 120 patients to discriminate between precancerous/cancerous and benign vocal cord tissue and reported sensitivity of 83% and specificity of 93% [54]. Finally, Chen et al. differentiated precancerous vs. benign oral lesions from 38 patients with 68% sensitivity and 95% specificity using in vivo time-resolved fluorescence spectroscopy (TRFS) [51]. Encouraged by these preceding studies, we hypothesized that widefield multispectral autofluorescence endoscopy imaging can enable new autofluorescence-derived features that can be used within a CAD system to automatically discriminate precancerous and cancerous oral lesions from benign oral epithelial tissue.

5.2 Methods

5.2.1 Multispectral Autofluorescence Image Database

The database used in this study included in vivo clinical endogenous multispectral autofluorescence images of 84 benign, 13 dysplastic (8 mild, 3 moderate, and 2 high-grade) and 35 cancerous (SCC) oral lesions from 125 patients previously acquired following the imaging protocol described in **subsection 2.2.1**.

5.2.2 Multispectral Autofluorescence Feature Computation

A total of 18 multispectral autofluorescence features were computed per image pixel, consisting in the multispectral intensity features described in **subsection 3.2.2** and their corresponding relative values obtained with **Equation 4.1**.

5.2.3 Image Classification and Performance Estimation

The multiparametric autofluorescence image dataset of 132 oral lesions was introduced into a classifier training and optimization process described in **subsection 3.2.3** and depicted in Figure 3.1.

5.3 Results

The classifier training performance for each of the six classifiers evaluated is presented in Figure 5.1. Because the LDA, QDA, DLDA, and DQDA classifiers yielded the same performance (sensitivity = 84%; specificity = 81%; accuracy = 82%), the LDA classifier was selected. The most frequently selected feature within the LOOCV process (Figure 3.1) was the normalized intensity in channel > 500 nm relative to Normal ($^{\Delta}I_{500,n}$). The optimized LDA posterior probability maps of the 132 oral lesions included in the dataset are presented in Figure 5.2. In these maps, each pixel represents a probability of belonging to the MALIGNANT class (SCC/HG-DYS).

The average image-level threshold on the percentage of positive pixels optimized within the LOOCV process and used to label each complete classification map as either BENIGN or MALIGNANT was $\sim$6% $\pm$ 0.3% as shown in Figure 5.3. The image-level classification obtained with the optimized LDA classifier versus the histopathological classification (gold standard) are compared in Table 5.1. The LDA classifier displayed levels of NPV of 93%, sensitivity and specificity of 84% and 81%, respectively, and overall accuracy of 82%.

5.4 Discussion

We designed and validated a computational framework for the classification of precancerous and cancerous vs. benign oral lesions based on multispectral autofluorescence endoscopy. In

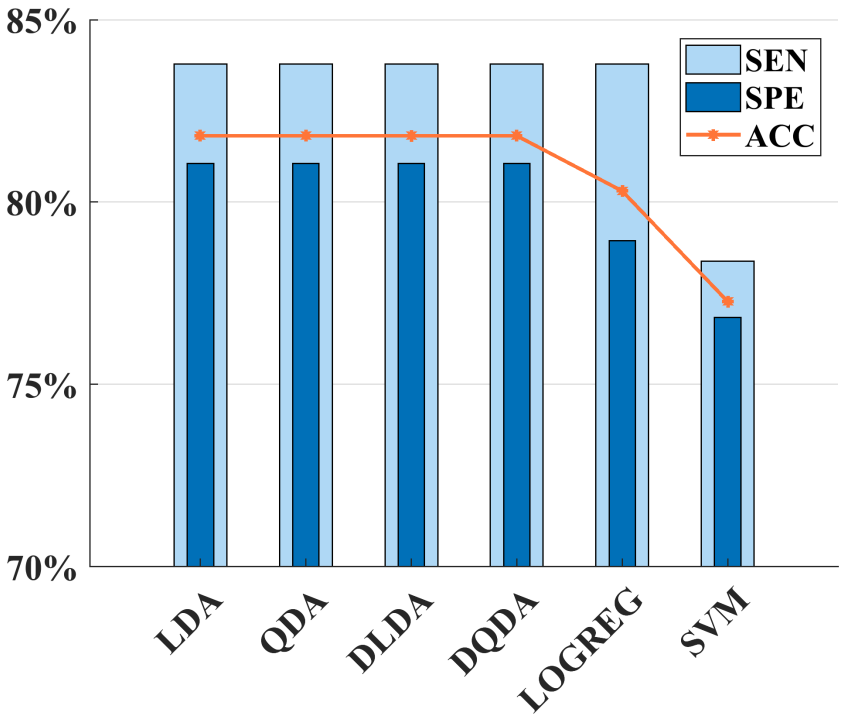

Figure 5.1: Classifier training performance. SEN: Sensitivity; SPE: Specificity; ACC: Accuracy.

this computational framework, a systematic selection of the best autofluorescence-derived feature ($^{\Delta}I_{500,n}$) was performed to optimize an LDA classifier that successfully discriminated SCC/HG-DYS oral lesions from Benign/MILD-DYS/MOD-DYS oral lesions.

The optimized LDA posterior probability maps of the 132 imaged oral lesions presented in Figure 5.2, indicate the pixel-level likelihood of malignancy and display evident contrast between high-grade dysplastic/SCC and benign oral tissues. The application of a threshold at 50% on the pixel-level posterior probabilities enabled the generation of binary classification maps from which the final label of the whole image was predicted using an optimized image-level threshold applied to the percentage of positive pixels. Cross-validated results from this image-level classification are summarized in Table 5.1. The optimized LDA classifier was able to correctly predict 77/95 benign oral lesions (67 Benign, 7 MILD-DYS, 3 MOD-DYS), and 31/37 malignant oral lesions (29 SCC, 2 HG-DYS). Nevertheless, 18 benign and 6 malignant oral lesions were misclassified. It can be noticed from Figure 5.2 that the missed positive cases present very small regions of red-colored

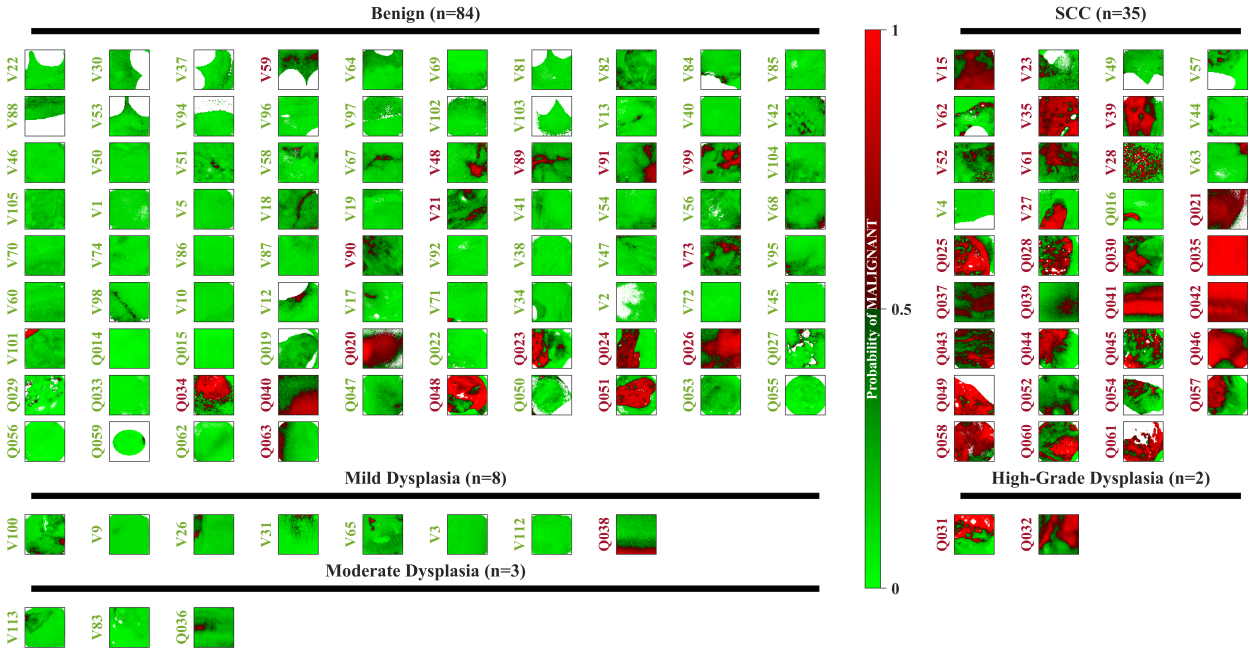

Figure 5.2: Posterior probability maps of 37 cancerous and precancerous oral lesions (SCC and High-Grade Dysplasia; right panels) and 95 benign oral lesions (Benign, Mild Dysplasia, and Moderate Dysplasia; left panels), obtained from an optimized cross-validated LDA classifier. Each pixel within these maps indicates a probability of MALIGNANT. Oral lesion identification numbers are shown on the left side of each probability map and color-coded red if MALIGNANT and green if BENIGN according to the predicted image-level classification.

pixels within their posterior probability maps, resulting in percentages of positive pixels below the optimized image-level threshold. In contrast, large red-colored regions were observed within the probability maps of the 6 missed negative cases. These regions are likely to indicate the presence of a highly-fluorescent superficial keratin layer that prevented the direct interrogation of the oral epithelium and affected its autofluorescence properties [20]. Another plausible explanation for this finding is that the autofluorescence properties of oral lesions can change based on their histologic diagnosis [49]. Therefore, combining different types of benign and dysplastic oral lesions in a single group, as performed in this study, might cause significant overlap with the autofluorescence features of the cancerous/high-grade dysplastic group, yielding false positives.

Recent in vivo autofluorescence imaging (AFI) and spectroscopy (AFS) studies in humans have reported promising findings in the discrimination of cancerous/precancerous vs. benign oral

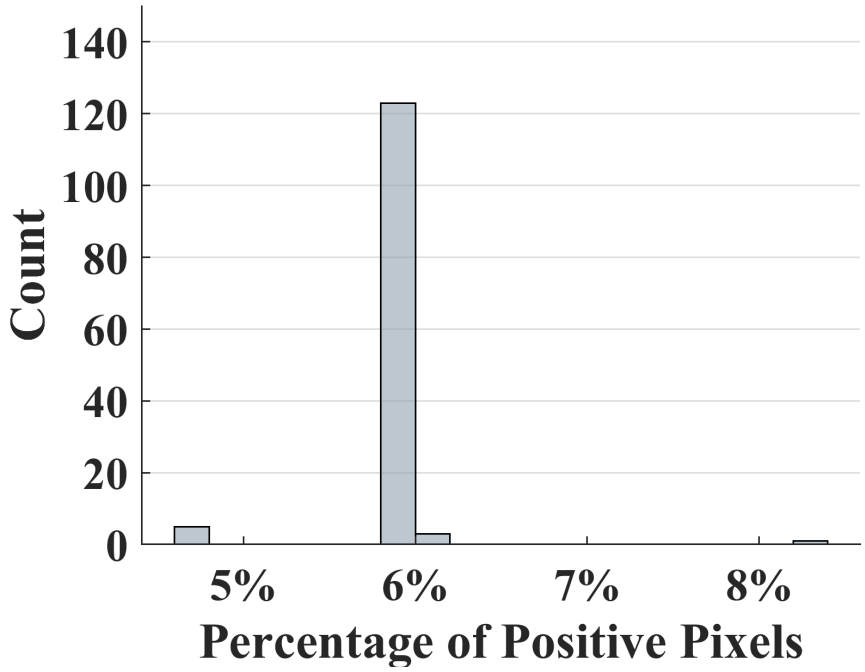

Figure 5.3: Distribution of optimal threshold on the percentage of positive pixels.

lesions as summarized in Table 5.2.

Kozakai et al. performed AFI in 50 patients using the Illumiscan® (SHOFU, Kyoto, Japan) fluorescence visualization device and reported levels of sensitivity and specificity of 85% and 93%, respectively in cancerous vs. benign oral lesions [55]. This study, however, did not include precancerous lesions in their classification problem and only investigated the discrimination of oral lichen planus from cancerous lesions, which might limit its clinical usefulness for the screening of other common types of benign oral lesions identified in patients. In our study, different categories of benign oral conditions were included in our classification task in addition to oral lichen planus, such as hyperplasia, hyperparakeratosis, fibroma, chronic mucositis, and mild/moderate dysplasia. As a result, the discriminatory capabilities of our computational framework could be more clinically relevant as they can be generalized on different types of benign oral lesions. In another study, Shi et al. performed AFI in 517 patients using the VELscope® and reported sensitivity and specificity of 72% and 39%, respectively in precancerous/cancerous vs. benign oral lesions [56]. Significantly higher levels of sensitivity and specificity of 84% and 81%, respectively for the

		Predicted		
		Benign/ MILD-DYS/MOD-DYS	**SCC/HG-DYS**	**Total**
True	**Benign**	67	17	84
	MILD-DYS	7	1	8
	MOD-DYS	3	0	3
	HG-DYS	0	2	2
	SCC	6	29	35
	Total	83	49	132

Table 5.1: Confusion matrix resulting from the LOOCV process. MILD-DYS: Mild Dysplasia, MOD-DYS: Moderate Dysplasia, HG-DYS: High-Grade Dysplasia, SCC: Squamous Cell Carcinoma.

Optical Modality	Number of Patients	Classification Task	Classification Performance	Reference
AFI (Illumiscan®)	50	CAN vs. BEN	SEN/SPE = 85%/93%	[55]
AFI (VELscope®)	517	PRE/CAN vs. BEN	SEN/SPE = 72%/39%	[56]
AFS	97	PRE/CAN vs. BEN/NOR	SEN/SPE = 81%/96%	[57]

Table 5.2: Summary of in vivo autofluorescence spectroscopy and imaging studies. AFI: Autofluorescence Imaging, AFS: Autofluorescence Spectroscopy, CAN: Cancer, PRE: Precancer, BEN: Benign, NOR: Normal, SEN: Sensitivity, SPE: Specificity.

same classification task were achieved with our multispectral autofluorescence endoscopy system coupled with an LDA classifier. The main advantages of our CAD system over the VELscope® are 1) the objective classification of the imaged oral lesions contrary to the subjective classification provided by the oral pathologist using the VELscope®, and 2) the integration of three spectral emission channels targeting the autofluorescence of collagen (390 $\pm$ 20 nm), NADH (452 $\pm$ 22.5 nm), and FAD (> 500 nm) for a more complete interrogation of the oral tissue autofluorescence, compared to the single broad spectral emission band (> 460 nm) used by the VELscope®. Finally, Wang et al. performed AFS in 97 patients and reported 81% sensitivity and 96% specificity in precancerous/cancerous vs. benign/normal oral tissues [57]. One limitation of this study is that all the imaged oral tissues belonged to the buccal mucosa, which might have facilitated the discrimination between cancerous/precancerous and benign/normal tissues due to the homogeneity of the dataset. Second, the relatively high specificity reported in this study could have benefited

from the combination of benign and normal oral tissues. Unfortunately, the classification of cancerous/precancerous vs. benign oral lesions alone was not investigated, which could have been relevant to enable a fair comparison with the levels of sensitivity and specificity achieved in our study.

5.4.1 Study Limitations

The classification results obtained in this study indicated that the optimized image-level threshold on the percentage of positive pixels is highly dependent on the size or extension of the imaged oral lesions. Even though the average optimal image-level threshold was very small ($\sim$6%), six cancerous lesions were misclassified as noticed in the LDA posterior probability maps from Figure 5.2. This limitation raises the need of an experienced oral pathologist to complement the discriminatory information provided by our CAD system and help determine if the imaged oral lesion warrants a biopsy. Another important limitation of this study is that the number of negative cases (n=95) included in our image database is more than twice the number of positive cases (n=37). This class imbalance might introduce a bias in the classifier towards the negative class, which has the largest number of samples. Future studies will focus on 1) assessing this class imbalance by imaging a larger number of positive cases and 2) further validating our computational framework on a testing dataset blinded to the classifier training and optimization stage.

In summary, this in vivo study in humans demonstrates the potential of widefield multispectral autofluorescence endoscopy for the automated classification of precancerous/cancerous vs. benign oral epithelial lesions. The cross-validated results reported in this study displayed clinically relevant levels of sensitivity and specificity. Nevertheless, the proposed computational framework needs to undergo further validation on a completely independent testing dataset to obtain a more accurate estimation of the lesion image classification performance. Once fully developed and validated, this innovative computational tool could aid in the clinical and non-invasive discrimination of malignant and premalignant oral lesions from benign oral tissue.

5.5 Conclusions

A computational framework was designed and developed for the classification of precancerous and cancerous vs. benign oral lesions based on multispectral autofluorescence endoscopy. The proposed framework successfully differentiated between benign/mild/moderate dysplastic lesions and oral high-grade dysplasia/SCC. Once fully validated clinically, this novel computational tool will serve as an optical diagnostic adjunct for the automated and in situ discrimination of cancerous/precancerous from benign oral lesions.

6. SUMMARY AND CONCLUSIONS

Two main challenges in the clinical diagnosis of oral epithelial cancer were addressed in this dissertation: The identification of positive resection margins and the early detection of cancerous oral lesions in patients.

Section 2 demonstrated the imaging and quantification of both established and potentially new biochemical and metabolic biomarkers of oral cancer through multispectral FLIM endoscopy. These autofluorescence biomarkers displayed contrast in precancerous and cancerous oral lesions vs. normal oral tissue. Subsequently, Section 3 reported the successful discrimination of precancerous/cancerous lesions from normal oral tissue by means of a computational framework based on multispectral autofluorescence endoscopy.

In Section 4, novel multispectral FLIM-derived autofluorescence biomarkers of oral cancer useful to distinguish cancerous and precancerous from benign oral lesions were clinically imaged and quantified. Afterwards, in Section 5, a multispectral autofluorescence endoscopy based computational framework was able to successfully distinguish precancerous/cancerous from benign oral lesions.

The findings reported in this work provide the basis for the use of widefield multispectral autofluorescence endoscopy as a novel non-invasive clinical tool for oral cancer screening. Once fully developed and validated, this tool will facilitate early detection and surgical margin demarcation, while reducing the number of unnecessary and painful oral tissue biopsy examinations.

REFERENCES

[1] *American Cancer Society: Cancer Facts and Figures*, 2020.

[2] Y. Sun, J. E. Phipps, J. Meier, N. Hatami, B. Poirier, D. S. Elson, D. G. Farwell, and L. Marcu, "Endoscopic fluorescence lifetime imaging for in vivo intraoperative diagnosis of oral carcinoma," *Microsc Microanal*, vol. 19, no. 4, pp. 791–8, 2013.

[3] J. J. Kain, A. C. Birkeland, N. Udayakumar, A. B. Morlandt, T. M. Stevens, W. R. Carroll, E. L. Rosenthal, and J. M. Warram, "Surgical margins in oral cavity squamous cell carcinoma: Current practices and future directions," *The Laryngoscope*, 2019.

[4] R. W. Smits, S. Koljenović, J. A. Hardillo, I. Ten Hove, C. A. Meeuwis, A. Sewnaik, E. A. Dronkers, T. C. Bakker Schut, T. P. Langeveld, and J. Molenaar, "Resection margins in oral cancer surgery: room for improvement," *Head and Neck*, vol. 38, no. S1, pp. E2197–E2203, 2016.

[5] M. D. Slooter, H. J. Handgraaf, M. C. Boonstra, L.-A. van der Velden, S. S. Bhairosingh, I. Que, L. M. de Haan, S. Keereweer, P. B. van Driel, and A. Chan, "Detecting tumour-positive resection margins after oral cancer surgery by spraying a fluorescent tracer activated by gamma-glutamyltranspeptidase," *Oral Oncology*, vol. 78, pp. 1–7, 2018.

[6] M. L. Hinni, A. Ferlito, M. S. Brandwein-Gensler, R. P. Takes, C. E. Silver, W. H. Westra, R. R. Seethala, J. P. Rodrigo, J. Corry, and C. R. Bradford, "Surgical margins in head and neck cancer: a contemporary review," *Head and Neck*, vol. 35, no. 9, pp. 1362–1370, 2013.

[7] M. Mair, D. Nair, S. Nair, S. Dutta, A. Garg, A. Malik, A. Mishra, R. S. KS, and P. Chaturvedi, "Intraoperative gross examination vs frozen section for achievement of adequate margin in oral cancer surgery," *Oral Surgery, Oral Medicine, Oral Pathology and Oral Radiology*, vol. 123, no. 5, pp. 544–549, 2017.

[8] L. J. DiNardo, J. Lin, L. S. Karageorge, and C. N. Powers, "Accuracy, utility, and cost of frozen section margins in head and neck cancer surgery," *The Laryngoscope*, vol. 110, no. 10, pp. 1773–1776, 2000.

[9] M. G. Müller, T. A. Valdez, I. Georgakoudi, V. Backman, C. Fuentes, S. Kabani, N. Laver, Z. Wang, C. W. Boone, and R. R. Dasari, "Spectroscopic detection and evaluation of morphologic and biochemical changes in early human oral carcinoma," *Cancer: Interdisciplinary International Journal of the American Cancer Society*, vol. 97, no. 7, pp. 1681–1692, 2003.

[10] A. T. Shah, M. D. Beckler, A. J. Walsh, W. P. Jones, P. R. Pohlmann, and M. C. Skala, "Optical metabolic imaging of treatment response in human head and neck squamous cell carcinoma," *PloS One*, vol. 9, no. 3, p. e90746, 2014.

[11] J. A. Jo, B. E. Applegate, J. Park, S. Shrestha, P. Pande, I. B. Gimenez-Conti, and J. L. Brandon, "In vivo simultaneous morphological and biochemical optical imaging of oral epithelial cancer," *IEEE Transactions on Biomedical Engineering*, vol. 57, no. 10, pp. 2596–2599, 2010.

[12] C. Gulledge and M. Dewhirst, "Tumor oxygenation: a matter of supply and demand," *Anticancer Research*, vol. 16, no. 2, pp. 741–749, 1996.

[13] R. Drezek, C. Brookner, I. Pavlova, I. Boiko, A. Malpica, R. Lotan, M. Follen, and R. Richards-Kortum, "Autofluorescence microscopy of fresh cervical-tissue sections reveals alterations in tissue biochemistry with dysplasia," *Photochemistry and Photobiology*, vol. 73, no. 6, pp. 636–641, 2001.

[14] N. Ramanujam, R. Richards-Kortum, S. Thomsen, A. Mahadevan-Jansen, M. Follen, and B. Chance, "Low temperature fluorescence imaging of freeze-trapped human cervical tissues," *Optics Express*, vol. 8, no. 6, pp. 335–343, 2001.

[15] B. Chance, B. Schoener, R. Oshino, F. Itshak, and Y. Nakase, "Oxidation-reduction ratio studies of mitochondria in freeze-trapped samples. nadh and flavoprotein fluorescence signals," *Journal of Biological Chemistry*, vol. 254, no. 11, pp. 4764–4771, 1979.

[16] Z. Zhang, D. Blessington, H. Li, T. M. Busch, J. D. Glickson, Q. Luo, B. Chance, and G. Zheng, "Redox ratio of mitochondria as an indicator for the response of photodynamic therapy," *Journal of Biomedical Optics*, vol. 9, no. 4, pp. 772–779, 2004.

[17] A. T. Shah, T. M. Heaster, and M. C. Skala, "Metabolic imaging of head and neck cancer organoids," *PloS One*, vol. 12, no. 1, p. e0170415, 2017.

[18] M. C. Skala, K. M. Riching, A. Gendron-Fitzpatrick, J. Eickhoff, K. W. Eliceiri, J. G. White, and N. Ramanujam, "In vivo multiphoton microscopy of nadh and fad redox states, fluorescence lifetimes, and cellular morphology in precancerous epithelia," *Proceedings of the National Academy of Sciences*, vol. 104, no. 49, pp. 19494–19499, 2007.

[19] I. Pavlova, K. Sokolov, R. Drezek, A. Malpica, M. Follen, and R. Richards-Kortum, "Microanatomical and biochemical origins of normal and precancerous cervical autofluorescence using laser-scanning fluorescence confocal microscopy," *Photochemistry and Photobiology*, vol. 77, no. 5, pp. 550–555, 2003.

[20] I. Pavlova, M. Williams, A. El-Naggar, R. Richards-Kortum, and A. Gillenwater, "Understanding the biological basis of autofluorescence imaging for oral cancer detection: high-resolution fluorescence microscopy in viable tissue," *Clin Cancer Res*, vol. 14, no. 8, pp. 2396–404, 2008.

[21] C. F. Poh, L. Zhang, D. W. Anderson, J. S. Durham, P. M. Williams, R. W. Priddy, K. W. Berean, S. Ng, O. L. Tseng, and C. MacAulay, "Fluorescence visualization detection of field alterations in tumor margins of oral cancer patients," *Clinical Cancer Research*, vol. 12, no. 22, pp. 6716–6722, 2006.

[22] T.-T. Huang, K.-C. Chen, T.-Y. Wong, C.-Y. Chen, W.-C. Chen, Y.-C. Chen, M.-H. Chang, D.-Y. Wu, T.-Y. Huang, and S. Nioka, "Two-channel autofluorescence analysis for oral cancer," *Journal of Biomedical Optics*, vol. 24, no. 5, p. 051402, 2018.

[23] U. Kanniyappan, A. Prakasarao, K. Dornadula, and G. Singaravelu, "An in vitro diagnosis of oral premalignant lesion using time-resolved fluorescence spectroscopy under uv excita-

tion—a pilot study," *Photodiagnosis and Photodynamic Therapy*, vol. 14, pp. 18–24, 2016.

[24] A. T. Shah and M. C. Skala, "Ex vivo label-free microscopy of head and neck cancer patient tissues," in *Multiphoton Microscopy in the Biomedical Sciences XV*, vol. 9329, p. 93292B, International Society for Optics and Photonics, 2015.

[25] J. D. Meier, H. Xie, Y. Sun, Y. Sun, N. Hatami, B. Poirier, L. Marcu, and D. G. Farwell, "Time-resolved laser-induced fluorescence spectroscopy as a diagnostic instrument in head and neck carcinoma," *Otolaryngology—Head and Neck Surgery*, vol. 142, no. 6, pp. 838–844, 2010.

[26] S. Cheng, R. M. Cuenca, B. Liu, B. H. Malik, J. M. Jabbour, K. C. Maitland, J. Wright, Y.-S. L. Cheng, and J. A. Jo, "Handheld multispectral fluorescence lifetime imaging system for in vivo applications," *Biomedical Optics Express*, vol. 5, no. 3, pp. 921–931, 2014.

[27] *Safe Use of Lasers: ANSI Z136.1–2007*, 2007.

[28] J. Lakowicz, *Principles of Fluorescence Spectroscopy*. Springer US, 2007.

[29] P. Lu, V. M. Weaver, and Z. Werb, "The extracellular matrix: a dynamic niche in cancer progression," *J Cell Biol*, vol. 196, no. 4, pp. 395–406, 2012.

[30] R. A. Drezek, K. V. Sokolov, U. Utzinger, I. Boiko, A. Malpica, M. Follen, and R. R. Richards-Kortum, "Understanding the contributions of nadh and collagen to cervical tissue fluorescence spectra: modeling, measurements, and implications," *Journal of Biomedical Optics*, vol. 6, no. 4, pp. 385–397, 2001.

[31] E. Gnanatheepam, U. Kanniyappan, K. Dornadula, A. Prakasarao, and G. Singaravelu, "Synchronous luminescence spectroscopy as a tool in the discrimination and characterization of oral cancer tissue," *Journal of Fluorescence*, vol. 29, no. 2, pp. 361–367, 2019.

[32] Y. Sun, J. Phipps, D. S. Elson, H. Stoy, S. Tinling, J. Meier, B. Poirier, F. S. Chuang, D. G. Farwell, and L. Marcu, "Fluorescence lifetime imaging microscopy: in vivo application to diagnosis of oral carcinoma," *Optics Letters*, vol. 34, no. 13, pp. 2081–2083, 2009.

[33] R. Sethupathi, K. Gurushankar, and N. Krishnakumar, "Optical redox ratio differentiates early tissue transformations in dmba-induced hamster oral carcinogenesis based on autofluorescence spectroscopy coupled with multivariate analysis," *Laser Physics*, vol. 26, no. 11, p. 116202, 2016.

[34] M. G. Vander Heiden, L. C. Cantley, and C. B. Thompson, "Understanding the warburg effect: the metabolic requirements of cell proliferation," *Science*, vol. 324, no. 5930, pp. 1029–1033, 2009.

[35] O. I. Kolenc and K. P. Quinn, "Evaluating cell metabolism through autofluorescence imaging of nad (p) h and fad," *Antioxidants and Redox Signaling*, vol. 30, no. 6, pp. 875–889, 2019.

[36] M. J. Serafino, B. L. Walton, M. Buja, J. Adame, B. E. Applegate, and J. Jo, "Cost-effective optical-reference-free frequency domain fluorescence lifetime imaging (flim) implementation using field programmable gate arrays (fpgas) for real time acquisition and processing," *Poster presented at: SPIE Photonics West 2018*, 2018.

[37] T. Hinsdale, C. Olsovsky, J. J. Rico-Jimenez, K. C. Maitland, J. A. Jo, and B. H. Malik, "Optically sectioned wide-field fluorescence lifetime imaging microscopy enabled by structured illumination," *Biomedical Optics Express*, vol. 8, no. 3, pp. 1455–1465, 2017.

[38] G. A. Grillone, Z. Wang, G. P. Krisciunas, A. C. Tsai, V. R. Kannabiran, R. W. Pistey, Q. Zhao, E. Rodriguez-Diaz, O. M. A'Amar, and I. J. Bigio, "The color of cancer: margin guidance for oral cancer resection using elastic scattering spectroscopy," *The Laryngoscope*, vol. 127, pp. S1–S9, 2017.

[39] Z. Hamdoon, W. Jerjes, G. McKenzie, A. Jay, and C. Hopper, "Optical coherence tomography in the assessment of oral squamous cell carcinoma resection margins," *Photodiagnosis and Photodynamic Therapy*, vol. 13, pp. 211–217, 2016.

[40] M.-J. Jeng, M. Sharma, L. Sharma, T.-Y. Chao, S.-F. Huang, L.-B. Chang, S.-L. Wu, and L. Chow, "Raman spectroscopy analysis for optical diagnosis of oral cancer detection," *Journal of Clinical Medicine*, vol. 8, no. 9, p. 1313, 2019.

[41] G. Nayak, S. Kamath, K. M. Pai, A. Sarkar, S. Ray, J. Kurien, L. D'Almeida, B. Krishnanand, C. Santhosh, and V. Kartha, "Principal component analysis and artificial neural network analysis of oral tissue fluorescence spectra: Classification of normal premalignant and malignant pathological conditions," *Biopolymers: Original Research on Biomolecules*, vol. 82, no. 2, pp. 152–166, 2006.

[42] M. A. Hall, "Correlation-based feature selection for machine learning," *The University of Waikato*, 1999.

[43] M.-J. Jeng, M. Sharma, T.-Y. Chao, Y.-C. Li, S.-F. Huang, L.-B. Chang, and L. Chow, "Multiclass classification of autofluorescence images of oral cavity lesions based on quantitative analysis," *PloS One*, vol. 15, no. 2, p. e0228132, 2020.

[44] P. Kumar, S. K. Kanaujia, A. Singh, and A. Pradhan, "In vivo detection of oral precancer using a fluorescence-based, in-house-fabricated device: a mahalanobis distance-based classification," *Lasers in Medical Science*, vol. 34, no. 6, pp. 1243–1251, 2019.

[45] T.-T. Huang, J.-S. Huang, Y.-Y. Wang, K.-C. Chen, T.-Y. Wong, Y.-C. Chen, C.-W. Wu, L.-P. Chan, Y.-C. Lin, and Y.-H. Kao, "Novel quantitative analysis of autofluorescence images for oral cancer screening," *Oral Oncology*, vol. 68, pp. 20–26, 2017.

[46] D. C. de Veld, M. Skurichina, M. J. Witjes, R. P. Duin, H. J. Sterenborg, and J. L. Roodenburg, "Clinical study for classification of benign, dysplastic, and malignant oral lesions using autofluorescence spectroscopy," *Journal of Biomedical Optics*, vol. 9, no. 5, pp. 940–951, 2004.

[47] J. B. Epstein, P. Güneri, H. Boyacioglu, and E. Abt, "The limitations of the clinical oral examination in detecting dysplastic oral lesions and oral squamous cell carcinoma," *The Journal of the American Dental Association*, vol. 143, no. 12, pp. 1332–1342, 2012.

[48] J. L. Cleveland and V. A. Robison, "Clinical oral examinations may not be predictive of dysplasia or oral squamous cell carcinoma," *J Evid Based Dent Pract*, vol. 13, no. 4, pp. 151–4, 2013.

[49] A. M. Gillenwater, B. Nadarajah Vigneswaran, and D. DrMedDent, "Noninvasive diagnostic adjuncts for the evaluation of potentially premalignant oral epithelial lesions: current limitations and future directions," *Oral and Maxillofacial Pathology*, 2018.

[50] M. W. Lingen, E. Abt, N. Agrawal, A. K. Chaturvedi, E. Cohen, G. D'Souza, J. Gurenlian, J. R. Kalmar, A. R. Kerr, and P. M. Lambert, "Evidence-based clinical practice guideline for the evaluation of potentially malignant disorders in the oral cavity: a report of the american dental association," *The Journal of the American Dental Association*, vol. 148, no. 10, pp. 712–727. e10, 2017.

[51] H. M. Chen, C. P. Chiang, C. You, T. C. Hsiao, and C. Y. Wang, "Time-resolved autofluorescence spectroscopy for classifying normal and premalignant oral tissues," *Lasers Surg Med*, vol. 37, no. 1, pp. 37–45, 2005.

[52] B. H. Malik, J. Lee, S. Cheng, R. Cuenca, J. M. Jabbour, Y. L. Cheng, J. M. Wright, B. Ahmed, K. C. Maitland, and J. A. Jo, "Objective detection of oral carcinoma with multispectral fluorescence lifetime imaging in vivo," *Photochemistry and Photobiology*, vol. 92, no. 5, pp. 694–701, 2016.

[53] K. Guze, H. C. Pawluk, M. Short, H. Zeng, J. Lorch, C. Norris, and S. Sonis, "Pilot study: Raman spectroscopy in differentiating premalignant and malignant oral lesions from normal mucosa and benign lesions in humans," *Head and Neck*, vol. 37, no. 4, pp. 511–517, 2015.

[54] X. Ni, J. Zhu, Q. Zhang, B. Zhang, and G. Wang, "Diagnosis of vocal cord leukoplakia: The role of a novel narrow band imaging endoscopic classification," *The Laryngoscope*, vol. 129, no. 2, pp. 429–434, 2019.

[55] A. Kozakai, K. Ono, T. Nomura, N. Takano, and T. Shibahara, "Usefulness of objective evaluations by fluorescence visualization device for differentiating between superficial oral squamous cell carcinoma and oral lichen planus," *Journal of Oral and Maxillofacial Surgery, Medicine, and Pathology*, vol. 32, no. 1, pp. 26–32, 2020.

[56] L. Shi, C. Li, X. Shen, Z. Zhou, W. Liu, and G. Tang, "Potential role of autofluorescence imaging in determining biopsy of oral potentially malignant disorders: A large prospective diagnostic study," *Oral Oncology*, vol. 98, pp. 176–179, 2019.

[57] C. Wang, T. Tsai, H. Chen, C. Chen, and C. Chiang, "Pls-ann based classification model for oral submucous fibrosis and oral carcinogenesis," *Lasers in Surgery and Medicine: The Official Journal of the American Society for Laser Medicine and Surgery*, vol. 32, no. 4, pp. 318–326, 2003.